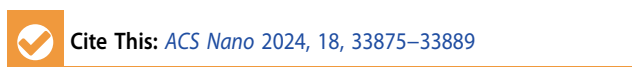
www.acsnano.org

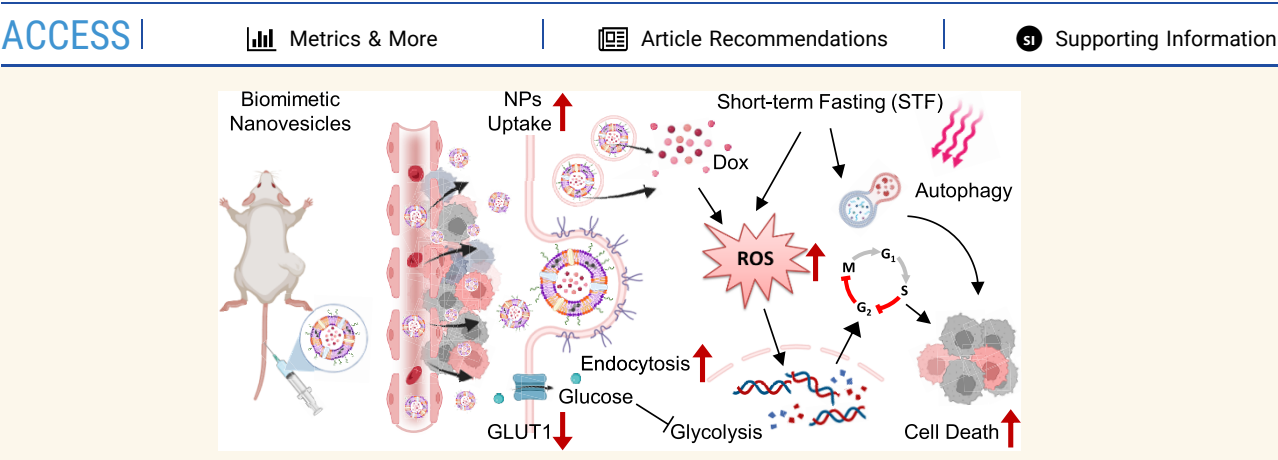
Downloaded via SHANGHAI JIAO TONG UNIV on December 19, 2024 at 11:39:57 (UTC). See https://pubs.acs.org/sharingguidelines for options on how to legitimately share published articles.

Biomimetic Nanovesicles Synergize with Short-Term Fasting for Enhanced Chemotherapy of Triple-Negative Breast Cancer

Seok Theng Chiang,[#] Qi Chen,[#] Tianzhen Han, Chunxi Qian, Xiaoshuai Shen, Yijing Lin, Rong Xu, Zhongyu Cao, Cheng Zhou, Haijiao Lu,^{*} Rongxiu Li,^{*} and Xiangzhao Ai^{*}







ABSTRACT: Triple-negative breast cancer (TNBC) is the most aggressive and lethal subtype of breast cancer among women. Chemotherapy acts as the standard regimen for TNBC treatment but suffers from limited drug accumulation in tumor regions and undesired side effects. Herein, we developed a synergistic strategy by combining a red blood cell (RBC) membrane-liposome hybrid nanovesicle with short-term fasting (STF) for improved chemotherapy of TNBC. The biomimetic nanovesicles exhibited reduced phagocytosis by macrophages while displaying a significant increase in tumor cell uptake through caveolae/raft-mediated endocytosis under nutrient-deprivation conditions. Importantly, drug-loaded nanovesicles and STF treatment synergistically increased the cytotoxicity of tumor cells by inhibiting their cell cycles and aerobic glycolysis as well as amplifying the reactive oxygen species (ROS) and autophagosomes generation. In the STF-treated mice, biomimetic nanovesicles greatly improved the antitumor efficacy at a lower drug dosage and inhibited the undesired metastasis of TNBC. Overall, we demonstrated that biomimetic nanovesicles synergizing with STF therapy serve as a promising therapeutic strategy for enhanced chemotherapy of malignant TNBC.

KEYWORDS: red blood cell membrane, biomimetic nanovesicles, short-term fasting, drug delivery, chemotherapy

Breast cancer is the most frequently diagnosed cancer globally. It remains the second-highest cause of cancer mortality among women in 2022, with an estimated 2.31 million new cases and 0.67 million deaths. Triple-negative breast cancer (TNBC) is characterized by the absence or low expression of the estrogen receptor, progesterone receptor, and human epidermal growth factor receptor 2 (HER-2). Compared to a hormone receptor and HER-2-overexpressed breast cancer, TNBC has long been considered to be the most aggressive and fatal subtype with a poor prognosis, accounting for approximately 15–20% of all breast carcinomas. The lack of recognized receptor

targets for therapy, patients with TNBC do not benefit from the current established endocrine or HER-2-targeted drugs.⁵ Thus, chemotherapy still remains the standard regimen for

Received: May 28, 2024
Revised: November 18, 2024
Accepted: November 25, 2024
Published: December 4, 2024





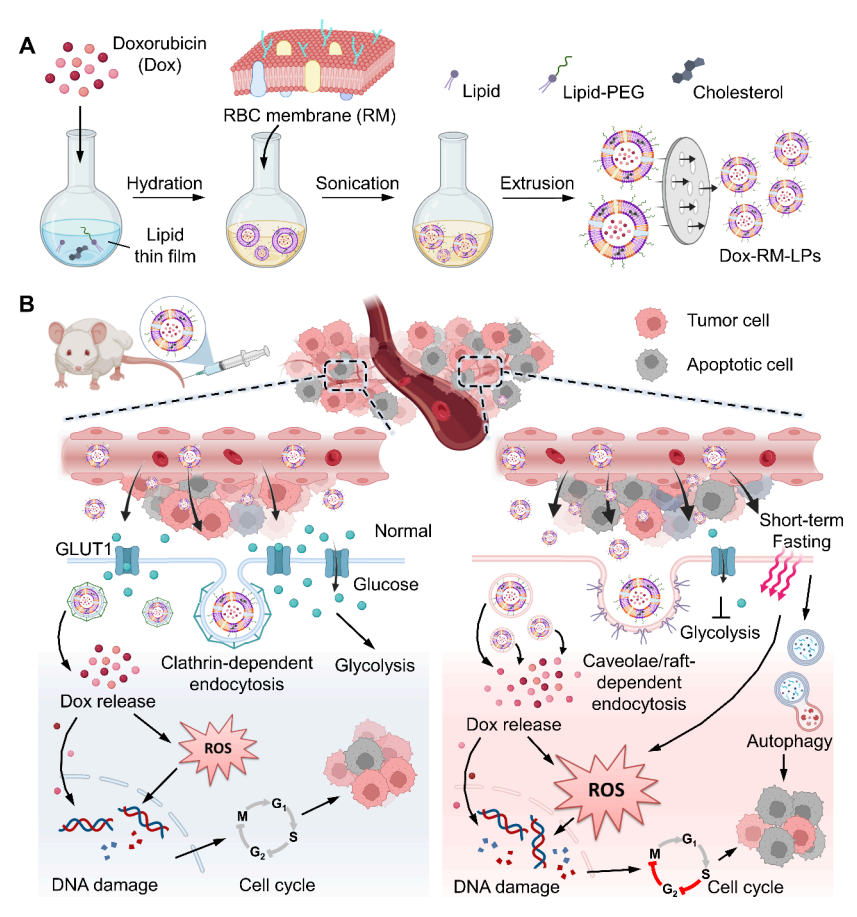


Figure 1. Schematic illustration of (A) biomimetic nanovesicle fabrication procedures and (B) mechanisms of drug-loaded nanovesicles synergizing with short-term fasting (STF) for enhanced chemotherapy of triple-negative breast cancer (TNBC).

TNBC treatment in both the early and advanced stages of the disease.⁶ Furthermore, dose-dense and high-dose treatment approaches are reported to be more effective in patients with TNBC.^{7,8} Unfortunately, frequent administration or high doses of chemotherapeutic drugs often lead to off-target toxicity, resulting in acute side effects (e.g., cardiotoxicity, hepatorenal toxicity, myelotoxicity, nausea, vomiting, etc.) and drug resistance.^{9–11} Therefore, innovative strategies are in great demand to promote drug accumulation in tumor regions and increase the therapeutic efficacy of TNBC with drugs at lower doses.

Nanotechnology-driven drug delivery systems (NDDS) have attracted much attention in the past few decades for cancer therapy as they provide innovative platforms to increase the potency of cancer treatments while minimizing the side effects of drug therapies. 12-23 Benefiting from the advantages of the enhanced permeability and retention (EPR) effect, it allows nanocarriers to accumulate in the tumor owing to its increased vascular permeability and impaired lymphatic drainage. This approach could improve the antitumor capacity of chemotherapeutic drugs and reduce their adverse reactions.²⁴ However, upon intravenous (i.v.) administration, rapid clearance of circulating nanocarriers by the mononuclear phagocyte system (MPS) alleviates their localization to the tumor regions, thus compromising the efficiency of drug delivery. 25-28 Red blood cells (RBCs) have emerged as a natural delivery vehicle to overcome MPS clearance on account of the presence of self-markers such as CD47, a "don't eat me" signal, to evade phagocytosis by macrophages.^{29–32} Inspired by this phenomenon, researchers developed a biomimetic nanoplatform by coating the RBC membrane on the surface of nanoparticles (NPs).^{31–33} With this strategy, RBC-camouflaged NPs combine the biological properties of RBC membranes with the advantages of synthetic NPs. These NPs possess desirable features of natural RBCs, including escaping macrophage uptake, prolonged blood circulation, and reduced immunogenicity.^{34–36} Despite the several advantages mentioned, there are still challenges that need to be overcome, including insufficient targeting and therapeutics at the tumor site.³⁷ Hence, emerging approaches are highly desired to compensate for the inherent defects of current NDDS and improve the efficiency of chemotherapeutic drugs in solid tumors, especially for TNBC.

Short-term fasting (STF) is one of the most commonly used dietary interventions in cancer treatment. STF often refers to episodic periods of restricted calorie consumption. ^{38–40} Growing preclinical evidence suggests that STF could play a key role in boosting the efficacy of chemotherapy. ^{41–43} STF differentially affects healthy cells compared to tumor cells by protecting healthy cells from being damaged by stressors such as chemotherapeutic drugs while sensitizing tumor cells toward cancer therapies. ^{44–49} The distinct response between healthy and tumor cells during nutrient restriction is defined as differential stress resistance. Upon nutrient deprivation, healthy cells downregulate the proliferation-associated genes and enter a self-maintenance or repair mode to avoid the damage of chemotherapy. ^{50,51} On the contrary, owing to the frequent mutations of tumor suppressor genes, tumor cells acquire the

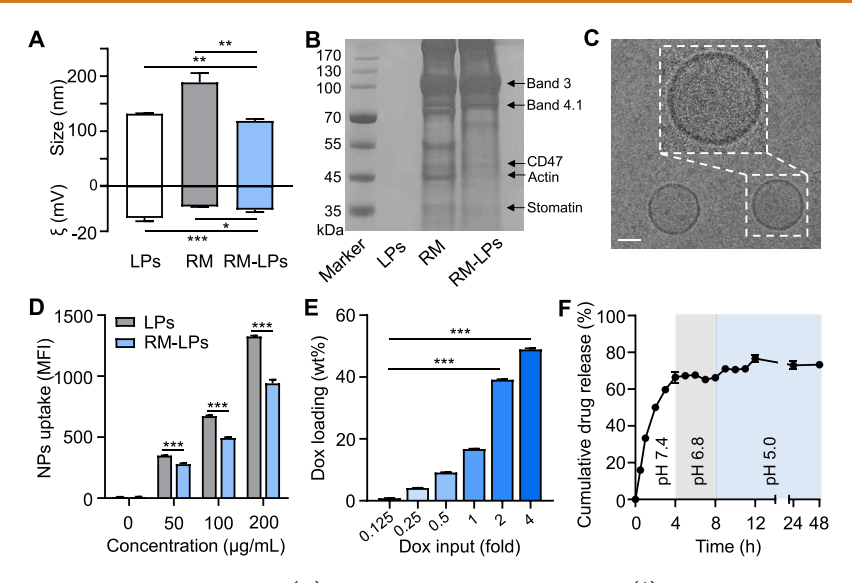


Figure 2. Preparation and characterization of RM-LPs. (A) Size and surface zeta potential (ξ) measurements of LPs, RM, and RM-LPs. (B) SDS-PAGE analysis of the membrane protein composition of RM and RM-LPs. (C) Cryo-EM imaging of RM-LPs. Scale bar: 50 nm. (D) Mean fluorescence intensity (MFI) of the RAW264.7 cell uptake of DiR-labeled NPs at different concentrations after 4 h of incubation. (E) Quantification of drug loading on RM-LPs with an increasing Dox input-to-NP weight ratios. (F) Sequential drug release profile of Dox-RM-LPs in the solutions at different pH values.

capability to sustain proliferative signaling even in the absence of growth factors. Additionally, tumor cells also exhibit aberrant metabolic activity that relies on aerobic glycolysis, resulting in high rates of glucose uptake and lactate production. This phenomenon is known as the Warburg effect, allowing tumor cells to sustain their cellular growth and proliferation during resource deprivation. Thus, STF is capable of inducing the anti-Warburg effect by depleting glucose levels in the tumor microenvironment, leading to tumor cell death and making them more vulnerable to chemotherapy. Moreover, STF therapy is generally safe and is well-tolerated. Only mild adverse events were reported, such as dizziness, fatigue, and short-term weight loss. Therefore, STF serves as a potential and simple strategy to synergistically improve the efficacy and tolerability of chemotherapeutic drugs.

The unique properties of STF inspire us to combine it with a biomimetic nanoplatform for the enhanced chemotherapy of TNBC. Herein, we designed RBC membrane-liposome hybrid nanovesicles (denoted "RM-LPs") to deliver doxorubicin hydrochloride (Dox), a hydrophilic antitumor drug widely used in clinics (Figure 1). Interestingly, we found that TNBC cells with STF treatment ingested more RM-LPs mainly through caveolae/raft-mediated endocytosis. The cytotoxicity of Dox-loaded RM-LPs (Dox-RM-LPs) was also significantly elevated in STF-treated tumor cells, along with the inhibition of aerobic glycolysis and the enhanced production of ROS and autophagosome. Animal studies confirmed that Dox-RM-LPs combined with STF treatment dramatically increased the antitumor efficacy of TNBC at lower Dox doses and inhibited the undesired tumor metastasis. Overall, we demonstrated that STF acts as a promising strategy to synergistically improve the drug delivery and chemotherapy efficacy of biomimetic nanomedicines against malignant TNBC.

RESULTS AND DISCUSSION

Preparation and Characterization of RM-LPs. In the study, RM-LPs were prepared using thin-film hydration, followed by an extrusion procedure. Purified RBC membrane

was isolated from mice whole blood based on hypotonic treatment followed by hybridization with synthetic lipids. Extrusion is one of the most commonly used methods for producing cell-membrane-coated NPs in the laboratory. However, it showed difficulty in achieving large-scale production due to the need for high extrusion pressure and loss of a sample caused by the deposition of materials on polycarbonate membrane filters after repeated extrusion. This procedure became much easier with the addition of lipids to the RBC membrane to improve its structural fluidity, which could particularly facilitate the artificial extrusion procedure of nanovesicle fabrication. RM-LPs were first fabricated with the addition of 10 wt % RBC membrane (denoted "RM") into the liposomes (denoted "LPs"). This nanoformulation had the best feasibility to promote the extrusion of cell membranes through the 100 nm polycarbonate membrane filters using a mini extruder. As shown in Figure 2A, dynamic light scattering (DLS) measurements revealed that the RM-LPs and LPs had comparable hydrodynamic diameters of 118.6 \pm 3.7 and 131.9 \pm 0.7 nm, respectively. These values were obviously lower than those of RM (188.6 \pm 17.0 nm), suggesting the feasible fabrication of RM-LPs by the extrusion process. Meanwhile, the surface zeta potential (ξ) of the RM-LPs (-10.5 \pm 1.1 mV) was distributed between the values of those in the LPs $(-14.1 \pm 1.4 \text{ mV})$ and RM $(-9.1 \pm 0.3 \text{ mV})$ groups, indicating the fusion of LPs with the cell membrane. The protein profiles of RM-LPs, RM, and LPs were also determined by using sodium dodecyl sulfate polyacrylamide gel electrophoresis (SDS-PAGE). Compared with RM and LPs, RM-LPs reserved almost all of their RBC cell membrane proteins reported previously, including band 3, band 4.1, CD47, actin, and stomatin (Figure 2B). When suspended in water, phosphate-buffered saline (PBS), and 50% fetal bovine serum (FBS), the sizes of RM-LPs remained unchanged over 5 days, implying their good colloidal stability (Figure S1). Furthermore, cryogenic electron microscopy (Cryo-EM) imaging of RM-LPs nanovesicles revealed a spherical structure and single lipid bilayer with a membrane thickness of 7.1 ± 0.7

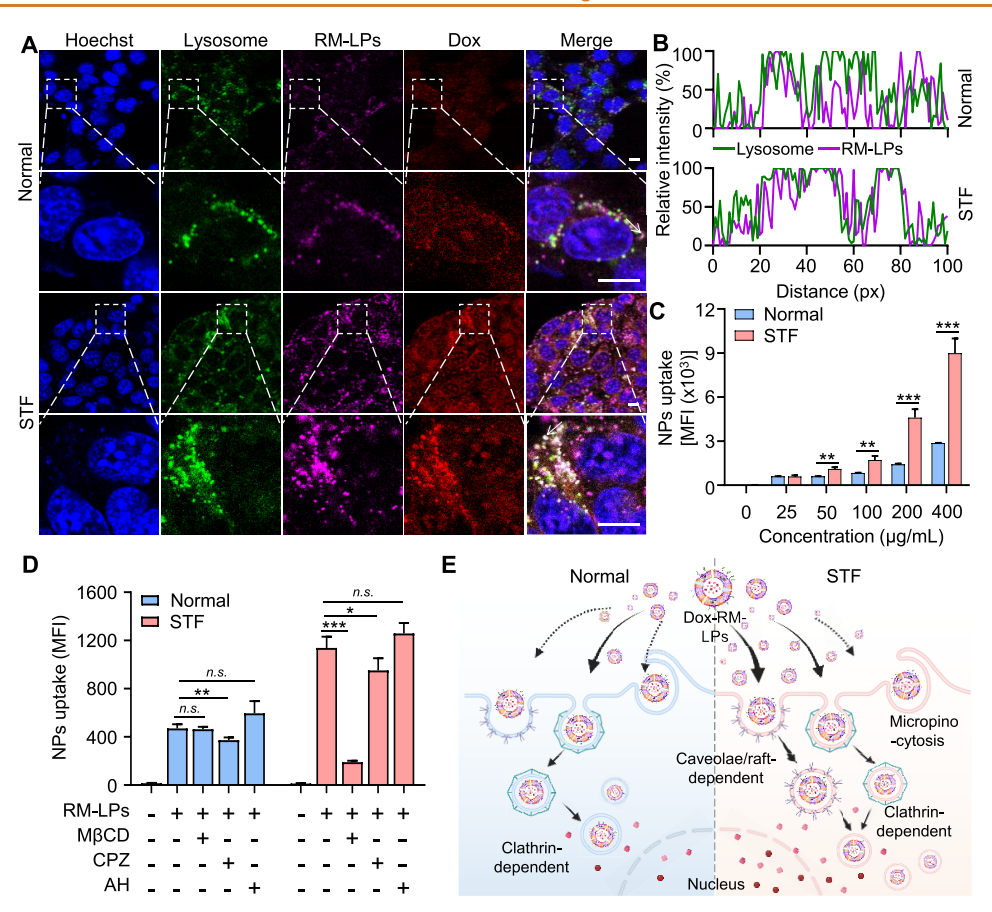


Figure 3. STF increases Dox-RM-LPs uptake in 4T1 TNBC cells primarily via caveolae/raft-mediated endocytosis. (A) Fluorescence images of 4T1 cells incubated with Dox-RM-LPs ($200 \,\mu\text{g/mL}$) for 4 h under normal and STF conditions. Scale bar: $10 \,\mu\text{m}$. (B) Colocalization curve of RM-LPs and the lysosome tracker in the normal and STF-treated 4T1 cells. (C) MFI of DiR-labeled RM-LP uptake in 4T1 cells with or without STF after 4 h of incubation. (D) MFI of DiR-labeled RM-LP uptake by 4T1 cells under normal or STF with different endocytosis inhibitors: methyl- β -cyclodextrin (M β CD, 5 mM), chlorpromazine-HCl (CPZ, 30 μ M), and amiloride hydrochloride (AH, 50 μ M). (E) Schematic illustration of the potential pathways of Dox-RM-LP endocytosis in 4T1 cells under normal and STF conditions.

nm (Figure 2C). These data demonstrated the successful fabrication of RM-LPs.

We then evaluated the functions of the RBC membrane in RM-LPs. The LPs without cell membrane hybridization were used as a control group. First, we determined the antiphagocytosis capabilities of RM-LPs and LPs on the RAW264.7 cell line, a murine macrophage that plays the primary cell model to engulf foreign NPs. To study the cellular uptakes of RM-LPs and LPs by macrophages, these NPs were first labeled with a hydrophobic fluorophore (DiR), followed by the incubation of different concentrations of DiR-labeled NPs with macrophages for 4 h, and the uptake was quantified with flow cytometry. As shown in Figure 2D, a lower level of phagocytosis was observed in the RM-LPs group when compared to the LP group. This result suggested that the RM-LPs could partly escape from macrophage uptake, probably attributed to the retention of CD47 from the RBC membrane, a self-marker protein that provides "don't eat me" signals to macrophages via interactions with the signal regulatory protein-alpha (SIRP- α) receptor. ^{30,58} To identify the immune-modulatory property of CD47, the RM-LPs were first incubated with anti-CD47 antibodies at a saturated concentration and quantified the cellular uptake by flow cytometry. As shown in Figure S2, the CD47-blocked RM-LPs resulted in an 83% recovery of NP internalization, revealing the immune-evasive capability of CD47 on biomimetic nanovasicles. We further studied the blood circulation properties of DiR-labeled RM, RM-LPs, and LPs upon i.v. injection into mice, followed by blood collection at different time points for fluorescence measurements. As shown in Figure S3, both of them have a nonlinear elimination curve. The apparent half-lives (denoted as 50% of the particles being cleared) of RM-LPs and LPs in the blood were 2.5 ± 0.3 and 2.7 ± 1.5 h, respectively, which were slightly lower than that in the RM-treated mice $(4.6 \pm 1.2 \text{ h})$ owing to the limited amounts of RBC membrane (10 wt %) on RM-LPs.

Next, a hydrophilic antineoplastic drug (Dox) was encapsulated into the core of the nanovesicles, and the drug loading and release properties were then determined. To optimize the Dox loading capacity of RM-LPs, the drug inputs were examined relative to the total weight of RM-LPs, and the loading amounts were quantified based on the specific absorbance of Dox at 480 nm. The particle sizes of Dox-RM-LPs exhibited a constant increase pattern with increasing concentrations of drug (Figure S4A). As shown in Figure 2E, the loading capacity of Dox in RM-LPs also increased with the drug input. Nevertheless, RM-LPs loaded with 2-fold Dox had the highest encapsulation rate at 23.5% (Figure S4B). Thus, we chose the 2-fold drug input with a drug loading capacity of 39.1 \pm 0.2 wt % for the following studies. To understand the drug release characteristics of Dox-RM-LPs in normal and tumor regions upon nanodrug administration in vivo, we

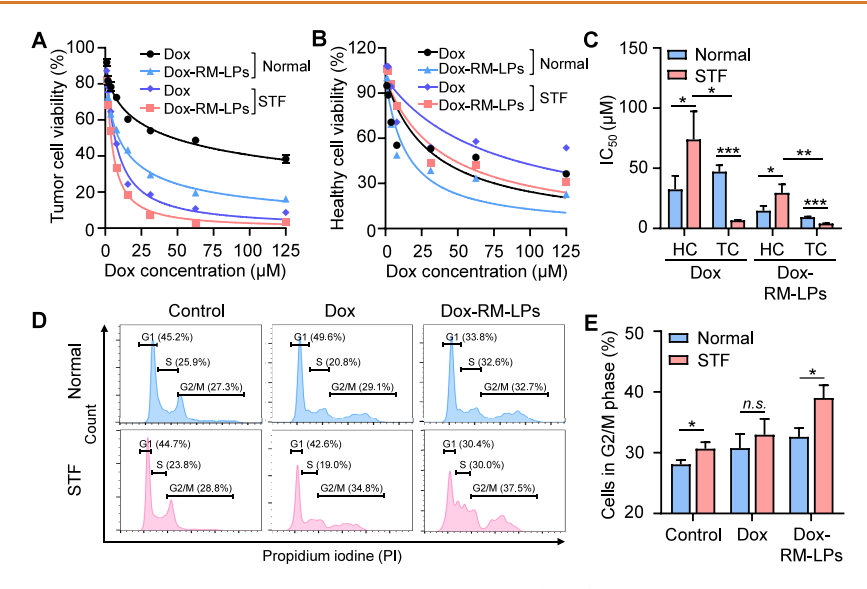


Figure 4. STF enhances the therapeutics effects of Dox-RM-LPs in tumor cells. (A, B) Cell viabilities of 4T1 tumor cells (A) and MODE-K healthy cells (B) with or without STF treatment upon incubation with various concentrations of free Dox and Dox-RM-LPs for 24 h. (C) Half-maximal inhibitory concentrations (IC_{50}) of Dox and Dox-RM-LPs against 4T1 tumor cells (TC) and MODE-K healthy cells (HC) under normal and STF conditions. (D, E) Flow cytometry analysis of the cell cycle (D) and the cell populations arrested at G2/M phases (E) in non- or STF-treated 4T1 cells upon exposure of free Dox or Dox-RM-LPs (4 μ M) for 24 h.

simulated and assessed the sequential drug release profiles of the Dox-RM-LPs at different pH levels to mimic the microenvironments of blood (pH = 7.4), the extracellular matrix in the tumor (pH = 6.8), and the intracellular lysosome (pH = 5.0), respectively. As shown in Figure 2F, a burst release of Dox from RM-LPs was observed at pH 7.4 during the initial 4 h and reached a plateau at pH 6.8 during the following 4 h. When the pH value decreased to 5.0 by adding the hydrochloric acid solution, a further increase in Dox release was determined from 66.2 ± 0.6 to $76.6 \pm 2.0\%$, suggesting the enhanced drug release profile after Dox-RM-LP uptake in the lysosome of tumor cells. The further release of Dox under acidic conditions was probably due to a differential between the extra-liposomal and intraliposomal pH values, which in turn drove an efflux of Dox from the liposome. 59 This provides an advantage for RM-LPs to promote lysosomal release of their content into the cytoplasm and allow the accumulation of drug molecules in tumor cells. We also analyzed the release kinetics by using a diffusion-dominant Higuchi model: $M_t = Kt^{1/2}$, where M_t is the amount of drug released at time t and K is the Higuchi constant, reflecting the release rate of drugs as a function of time (Figure S5).⁶⁰ Plotting the percentage of Dox released against the square root of time resulted in linear fitting curves with $R^2 = 0.98$, 0.02, and 0.75 for the RM-LPs under different pH conditions. The goodness of the curve fitting suggested a diffusion-controlled release of drugs in the neutral rather than the acid conditions. Based on this analysis, the Higuchi constant of the Dox released from RM-LPs was determined to be 34.6 \pm 0.5 h^{-1/2} at pH 7.4, 0.5 \pm 0.4 h^{-1/2} at pH 6.8, and 4.4 \pm 0.3 h^{-1/2} at pH 5.0.

Cellular Uptake Mechanism of Dox-RM-LPs during STF. Following the characterization of RM-LPs, we then investigated the mechanisms of NPs' cellular uptake under nutrient restriction in TNBC cells. In this study, 4T1 murine breast tumor cells, the most commonly used cell model of TNBC, were first cultured in a medium with low glucose (0.5 g/L) and FBS (1%) to mimic the STF condition or in a normal medium containing high glucose (2 g/L) and FBS (10%) as a

control group. To visualize the cellular uptake and intracellular transport pathways of RM-LPs and Dox by 4T1 cells, the RM-LPs nanovesicles were first labeled with a liposome-membranetargeting fluorogenic probe, and Dox-loaded RM-LPs were incubated with either normal or STF-treated tumor cells for 4 h, followed by confocal imaging. The released Dox was imaged based on its autofluorescence. As shown in Figure 3A,B and Figure S6, the fluorescence of RM-LPs was mainly colocalized with the green fluorescence signal of the lysosome tracker, suggesting that the RM-LPs were trapped in the lysosome both in normal and STF conditions during the endocytosis process. However, the red fluorescence signal of Dox was widely observed in the lysosome, nucleus, and cytoplasm, indicating the continuous release of Dox from RM-LPs in tumor cells. Importantly, both of the fluorescence signals of RM-LPs and Dox in the STF group were significantly higher when compared to those in the control group, revealing an elevated endocytosis of Dox-RM-LPs in tumor cells during starvation. The uptake efficiency of RM-LPs in 4T1 cells upon normal or STF treatment was also quantified by flow cytometry analysis. As shown in Figure 3C, the intracellular fluorescence intensity enhanced with the increasing of DiR-labeled RM-LPs concentrations, suggesting a dose-dependent cellular uptake of RM-LPs. At all concentrations, the signals in the STF group were significantly higher than those in the normal group, indicating an increased level of cellular uptake of RM-LPs under nutrient-deprivation conditions.

To further understand the endocytosis mechanism between the normal and STF groups, different endocytosis inhibitors were employed. These inhibitors included methyl- β -cyclodextrin (M β CD), chlorpromazine (CPZ), and amiloride hydrochloride (AH), which could specifically inhibit the caveolae/raft-dependent endocytosis, clathrin-dependent endocytosis, and micropinocytosis, respectively. Inhibitors were first pretreated with 4T1 cells before the incubation with DiRlabeled RM-LPs for 4 h. As shown in Figure 3D, under normal conditions, the uptake of RM-LPs was slightly suppressed when the tumor cells were pretreated with CPZ, while no

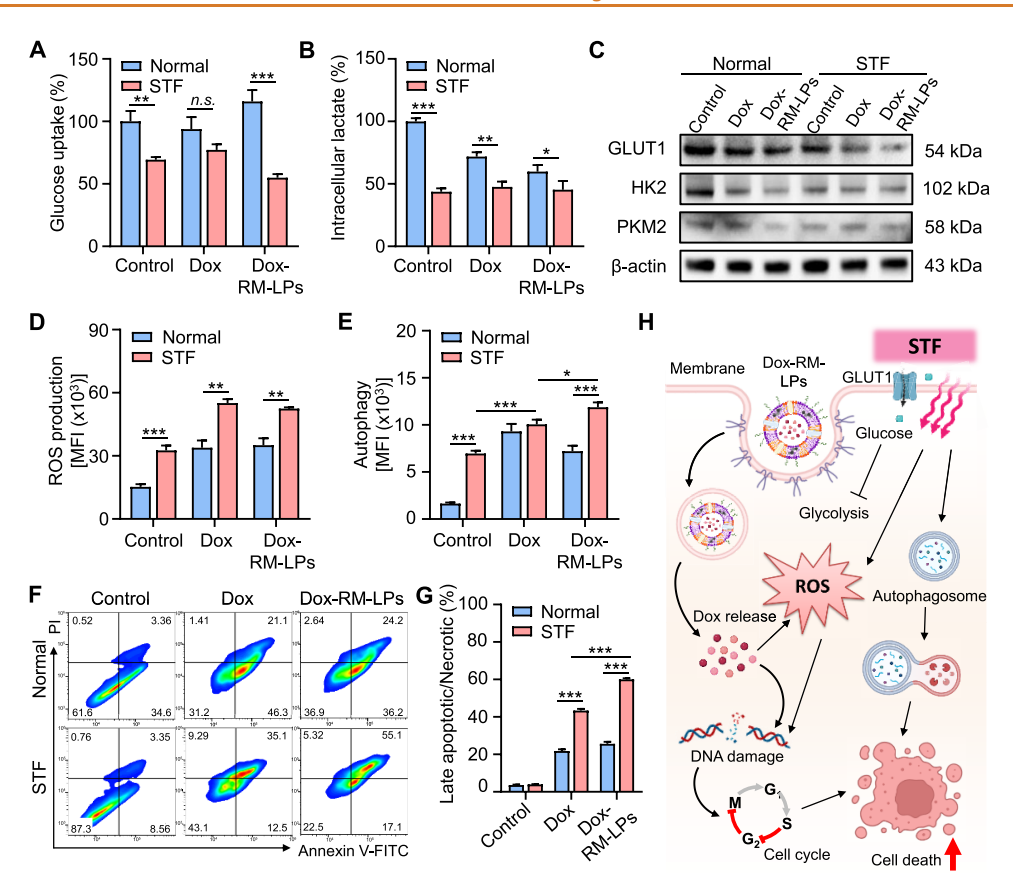


Figure 5. Mechanisms of Dox-RM-LPs synergizing with STF for enhance chemotherapy in tumor cells. (A, B) Relative levels of glucose uptake (A) and lactate production (B) in normal or fasted 4T1 cells. (C) Western blot analysis of glycolytic enzymes expression in glucose metabolism (GLUT1, HK2, and PKM2) during normal or STF conditions. (D, E) MFI of ROS (D) and autophagy (E) formation in normal or fasted 4T1 cells upon the treatment of free Dox or Dox-RM-LPs at the same conditions. (F, G) Flow cytometric assessment of apoptosis (F) and percentages of cell death (G) by the Annexin V-FITC/PI apoptotic assay in normal or STF-treated tumor cells. (H) Schematic diagram of tumor cell death with Dox-RM-LP treatment under normal and STF conditions.

significant difference was observed in the M β CD- and AH-treated cells. Conversely, upon STF treatment, the uptake of RM-LPs was dramatically reduced when the cells were preincubated with M β CD while exhibiting a slight suppression after CPZ addition. Previous studies have reported an enhanced uptake of extracellular lipid sources to fuel the cellular activities when cells were cultured in a nutrient-limited medium, while caveolae is associated with lipid uptake and metabolism. G2,63 Together, these results demonstrated that the cellular uptake of RM-LPs was initiated via clathrin-dependent endocytosis under normal conditions but underwent a caveolae/raft-mediated endocytosis process during STF treatment (Figure 3E).

STF Enhances the Therapeutics of Dox-RM-LPs In Vitro. Next, we studied the antitumor efficacy of Dox-RM-LPs in vitro. We hypothesize that the enhanced uptake of Dox-RM-LPs in the STF environment could improve their cytotoxicity in tumor cells. To test this hypothesis, 4T1 TNBC cells were first cultured in the normal or STF medium and treated with the same amounts of free Dox or Dox-RM-LPs for the cell viability assay. As shown in Figure 4A, the cell viability of tumor cells in both Dox and Dox-RM-LP groups gradually decreased with increased drug dosages. At all concentrations, the tumor cells with Dox-RM-LP treatment remained a cytotoxicer than the free Dox-treated groups, attributable to the augmented uptake levels of hydrophilic drugs by endocytosis when they were encapsulated in the NPs.

Importantly, the half-maximal inhibitory concentration (IC_{50}) value of 4T1 cells cultured with Dox-RM-LPs upon STF treatment (4.1 \pm 0.2 μ M) was greatly lower than that in the normal group (9.4 \pm 0.5 μ M) due to the enhanced uptake of RM-LPs by tumor cells during starvation. As evidence showed that STF able to protect normal cells from the toxic effects of chemotherapeutic drugs, 44-49 we further evaluated the cytotoxicities of free Dox and Dox-RM-LPs in a widely used healthy cell model (murine enterocyte cells, MODE-K) with or without STF treatment. As shown in Figure 4B, the viability of healthy cells treated with Dox-RM-LPs was also lower than that of the free Dox-treated groups at the same concentrations, mainly due to the enhanced uptake of drugs loaded into the RM-LPs. Under STF conditions, the IC₅₀ value of healthy cells with Dox (74.0 \pm 23.3 μ M) and Dox-RM-LP (29.5 \pm 7.1 μ M) treatment was greatly higher than that in the normal group treated with Dox (32.4 \pm 11.3 μ M) and Dox-RM-LPs (14.7 \pm 3.9 μ M) (Figure 4C). These results confirmed that STF could synergistically sensitize tumor cells to chemotherapy while protecting healthy cells during Dox-RM-LP treatment. This phenomenon was defined as differential stress resistance reported previously, probably attributable to the downregulation of proliferation-associated genes in the healthy cell rather than the tumor cells during starvation. 44,45 Moreover, the RM-LPs showed a negligible cytotoxicity effect on 4T1 cells and MODE-K cells, implying the great cellular safety of drug carriers in the normal or STF conditions (Figure S7).

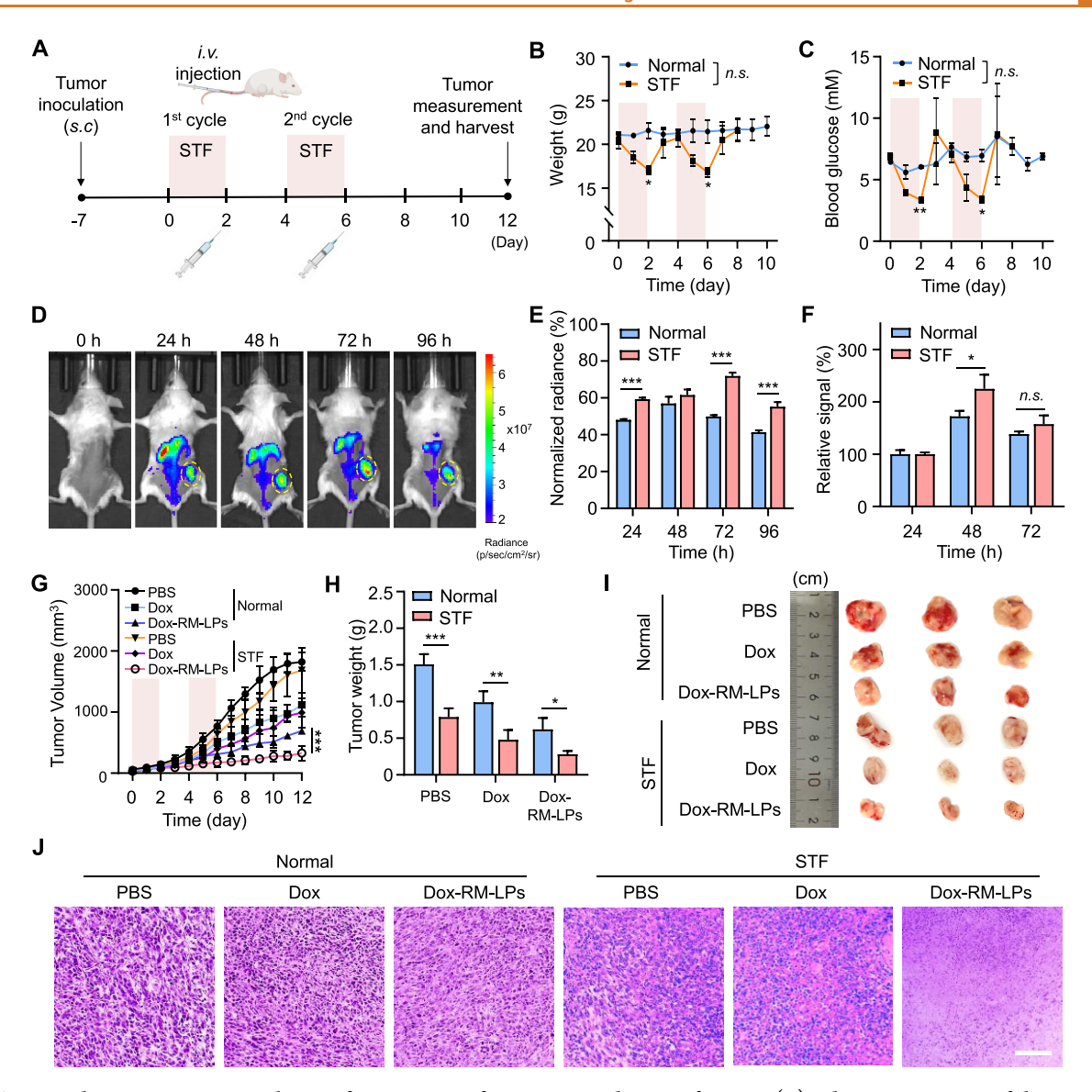


Figure 6. STF enhances tumor accumulation of Dox-RM-LPs for synergistic therapy of TNBC. (A) Schematic overview of the experimental timeline for the *in vivo* study. The pink area indicates the time frame of fasting treatment. (B, C) Body weights (B) and blood glucose level (C) of mice under normal or STF conditions. (D, E) *In vivo* imaging (D) and normalized fluorescence radiance (E) of 4T1 tumor-bearing mice after injection of DiR-labeled RM-LPs at 24, 48, 72, and 96 h in the STF-treated group. The yellow circle dashed lines indicate the tumor region. (F) Relative signals of DiR-labeled RM-LPs in 4T1 tumors based on *ex vivo* images. (G–I) Tumor growth curve (G), tumor weights (H), and tumor images (I) of 4T1 tumors in mice under different therapeutic regimes. (J) Representative H&E images of 4T1 tumor sections in various groups. Scale bar: 200 μ m.

Overall, these results demonstrated that STF is able to increase the cytotoxicity of Dox-RM-LPs against tumor cells.

We then investigated the mechanism of tumor cell death under both normal and STF conditions. As Dox treatment is involved in the disruption of DNA replication, we first studied the cell cycle of normal or STF-treated tumor cells using the propidium iodide (PI) staining method. Normally, the cells respond to extrinsic stimuli of proliferation and enter the cell cycle from gap 1 (G1), a phase in which the cells synthesize mRNA and proteins in preparation for subsequent steps leading to mitosis. After that, the cells replicate their DNA during the synthesis (S) phase and then move to the gap 2 (G2) phase to condense the chromatin into chromosomes and prepare necessary proteins for cell proliferation. The mitotic (M) phase is the last but the shortest period of the cell cycle, where cell division occurs to generate two identical daughter

cells.⁶⁴ As shown in Figure 4D, in the normal group, the percentages of cells arrested at G2/M phases were slightly higher in the free Dox (30.8%) and Dox-RM-LP (32.6%) groups than in the control cell (28.1%) due to Dox-induced DNA damage. However, in the STF group, G2/M phase-arrested cells were significantly augmented in the control (30.7%), free Dox (33.0%), and Dox-RM-LP (39.0%) groups, denoting the elevated inhibition of cell cycles during starvation (Figure 4E). Together, these results indicated that Dox-RM-LPs synergizing with STF treatment could significantly inhibit the proliferation of tumor cells.

To further investigate its cytotoxic mechanisms, we explored the impact of STF on aerobic glycolysis, a primary bioenergetic pathway of tumor cell growth. The levels of glucose uptake and lactate production, two main indicators of the Warburg effect, were determined using commercialized assay kits. As shown in Figure 5A,B, the glucose uptake and lactate production in tumor cells were dramatically reduced upon STF treatment in all of the groups. Similar reductions were also observed for the intracellular detection of glucose and adenosine triphosphate (ATP) in tumor cells cultured in a nutrient-limited medium (Figure S8). We further examined the levels of several key ratelimiting enzymes in glucose metabolism, including glucose transporter 1 (GLUT1, transporting of glucose across the plasma membranes), hexokinase 2 (HK2, catalyzing the glucose phosphorylation), and pyruvate kinase M2 (PKM2, converting phosphoenolpyruvate to pyruvate for ATP production). So As shown in Figure 5C, the Western blot results revealed a decreased expression of these glycolytic enzymes in the STF group when compared to the control group under normal conditions, especially for the significant downregulation of GLUT1. These results indicated that STF plays a critical role in inhibiting the aerobic glycolysis in TNBC cells. In addition, the intracellular ROS (e.g., superoxide radical and hydrogen peroxide) was detected based on the fluorogenic assay of dihydroethidium (a superoxide radical indicator) by flow cytometry. As expected, the ROS levels dramatically increased in the 4T1 cells during the STF treatment (Figure 5D). The addition of free Dox or Dox-RM-LPs further boosted ROS generation, leading to drug-induced cell damage both in normal and STF groups. Moreover, ROS-induced autophagy is a cellular protective pathway to alleviate oxidative stress, while excessive ROS could be a destructive process in tumor cells. 65,66 Therefore, we asked whether autophagy was involved in the enhanced cytotoxicity under nutrient-deprivation conditions. To this aim, monodansylcadaverine (MDC), an autofluorescent compound, was utilized for specifically labeling the autophagosomes in tumor cells. Indeed, an upregulation of MDC fluorescence in 4T1 cells of all groups was observed upon STF treatment, suggesting the enhanced production of autophagosomes in TNBC cells with limited nutrients (Figure 5E). A higher level of autophagy induction was further detected when the tumor cells were treated with free Dox or Dox-RM-LPs at a lower concentration (4 μ M). To further validate the contribution of programmed cell death by RM-LPs under fasting conditions, cell apoptosis was determined using Annexin V-FITC and a propidium iodide (PI) staining assay. As shown in Figure 5F,G, the percentage of late apoptotic (Annexin V⁺/PI⁺) and necrotic (Annexin V⁻/PI⁺) cells were significantly increased in the STF condition when compared to cells under the normal group. Notably, higher levels of apoptosis and necrosis were determined when the tumor cells were exposed to Dox-RM-LPs rather than free Dox due to the enhanced drug uptake efficiency. Collectively, these results confirmed that Dox-RM-LPs could significantly increase the cytotoxicity at lower doses, especially in the nutrientdeprivation conditions, mainly related to the elevated inhibition of DNA replication and aerobic glycolysis, as well as amplifying the reactive oxygen species (ROS) and autophagosomes production in TNBC cells (Figure 5H).

STF Improves Antitumor Efficacy of Dox-RM-LPs. Before evaluating the antitumor effect of Dox-RM-LPs in vivo, we first established the animal model of malignant TNBC for STF treatment based on the schedule described previously. The 4T1 tumor-bearing mice were first fasted for 48 h, followed by a sufficient food supply for another 48 h. Dox-RM-LPs were then injected via the tail vein at the end of each fasting cycle. A total of two cycles of fasting were conducted in this study (Figure 6A). To confirm the STF model induction

in vivo, the body weights and blood glucose concentrations of the mice were recorded every day. As shown in Figure 6B, the weights decreased during each fasting cycle but rapidly recovered to a healthy level after feeding with normal diets. In addition, the levels of blood glucose in mice decreased during STF but returned to normal levels after the food supply was resumed (Figure 6C). To further study the tumor accumulation of RM-LPs during each fasting cycle, DiRlabeled RM-LPs were i.v. administrated to determine the fluorescence imaging of tumor-bearing mice at the desired time points. As shown in Figure 6D,E, the fluorescence signal gradually increased at the tumor site within 96 h upon STF treatment, indicating effective tumor accumulation based on the EPR effect. Notably, the blood elimination of the nanocarrier was faster than their tumor accumulation due to the EPR effect.⁶⁷ This phenomenon might be attributed to the reported facts that the rate constants associated with exchange in the peripheral compartment during blood circulation were significantly higher than the rate constants for exchange in the tumor compartment. To confirm these observations, we then harvested tumors from mice at different time points for ex vivo imaging. The relative fluorescence signal at 48 h in the STFtreated tumor exhibited a significant augmentation (224.8 ± 27.1%) compared to the normal group (172.3 \pm 10.4%) when normalized to the signal at 24 h (Figure 6F and Figure S9). These results demonstrated that STF enhanced the tumor accumulation of NPs, which is important for NDDS.

Subsequently, we studied the pharmacokinetic profiles of free Dox and Dox-RM-LPs after i.v. injection in mice followed by blood collection at different time points for fluorescence measurements. As shown in Figure S10, the elimination halflives of free Dox and Dox-RM-LPs in the blood were calculated as 3.1 ± 0.1 and 3.8 ± 0.2 h in the blood, respectively, revealing an improved pharmacokinetics of chemotherapy drugs after loading into the nanocarrier. We then evaluated the therapeutic efficiency of Dox-RM-LPs in 4T1 cell-bearing mice without or with STF treatment. In the study, both STF-treated and normal mice were received two i.v. injections of Dox-RM-LPs or free Dox at a lower dosage (5 mg/kg). As shown in Figure 6G, when compared to the mice treated with PBS in the normal group, substantial inhibition of tumor growth was determined upon free Dox (41.9% decrease) and Dox-RM-LP (65.8% decrease) treatment at the same dosages. Importantly, further shrinkages in overall tumor volumes were observed upon administration of free Dox (47.8% decrease) and Dox-RM-LPs (85.7% decrease) in the STF-treated mice. These results presented the synergistic antitumor effects of Dox-RM-LPs at lower drug dosage in the mice due to the enhanced tumor accumulation and nutrient restriction. Such antitumor efficacy was further confirmed with tumor weights and images at the end point of the experiments. As shown in Figure 6H,I, the average weight and size of tumor tissues were significantly reduced in the mice upon Dox-RM-LP treatment, especially in the STF-mediated group. Notably, extensive necrosis of cells was observed in the tumor sections upon Dox-RM-LP treatment in the STF-treated mice, while limited cell damage was noticed in other control groups compared to that in the PBS-treated mice (Figure 6]). Altogether, the combination of Dox-RM-LPs and STF provided enhanced chemotherapy efficacy in tumor-bearing mice.

To evaluate the safety during treatment processes, body weights, blood tests, and pathological analyses were performed accordingly. As shown in Figure S11, the body weights of

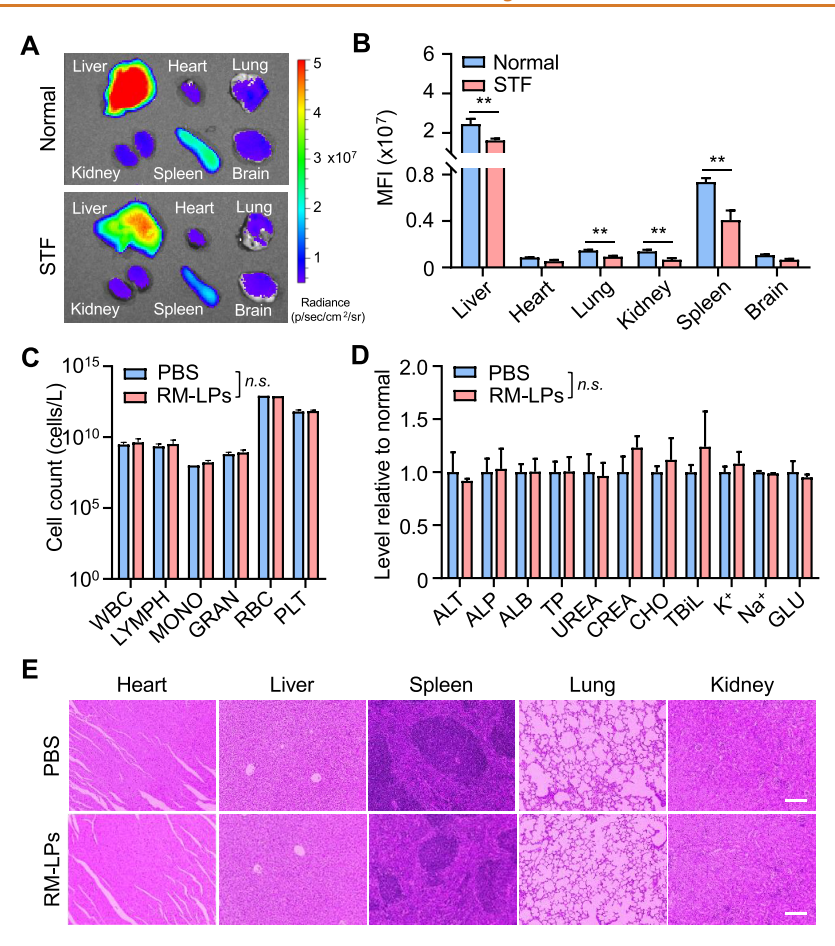


Figure 7. Biodistribution and biosafety studies of RM-LPs in vivo. (A, B) Distribution (A) and MFI (B) of main organs after DiR-labeled RM-LPs (20 mg/kg) injection into mice for 48 h under normal or STF conditions. (C) Amount of blood cells at day 7 after i.v. injection of PBS or RM-LPs. WBC, white blood cells; LYMPH, lymphocytes; MONO, monocytes; GRAN, granulocytes; RBC, red blood cells; PLT, platelets. (D) Comprehensive blood chemistry parameters at day 7 after i.v. injection with PBS or RM-LPs. ALT, alanine transaminase; ALP, alkaline phosphatase; ALB, albumin; TP, total protein; CRE, creatinine; CHO, cholesterol; TBiL, total bilirubin; K^+ , potassium; Na^+ , sodium; GLU, glucose. (E) H&E staining of main organs (heart, liver, spleen, lung, and kidneys) at day 7 after PBS or RM-LP administration. Scale bar: 200 μ m.

tumor-bearing mice with PBS, free Dox, and Dox-RM-LP treatment maintained stable in the normal groups due to their limited toxicity at a lower dosage. Upon STF treatment, the body weights of tumor-bearing mice underwent a short-term decrease during the fasting cycle and recovered to the normal weights after food supply. Moreover, the major organs and tumor tissues in different groups were further excised for hematoxylin and eosin (H&E) staining (Figure S12). Metastatic foci in the liver were observed in the PBS-treated mice but dramatically reduced in the Dox-treated mice and completely eliminated in the Dox-RM-LP-treated groups, suggesting the Dox-RM-LPs could inhibit the hepatic metastases of TNBC cells both in normal and STF conditions. Similarly, the lung metastasis with thickened alveolar walls in the tumor-bearing mice was also prohibited upon Dox-RM-LP treatment especially after nutrient starvation. The sections from other organs, such as the heart, spleen, and kidneys, revealed no significant changes in histopathology among all groups. These results demonstrated that Dox-RM-LPs synergizing with STF could significantly inhibit undesired tumor metastasis in the liver and lung. Furthermore, a blood count and comprehensive metabolic panel were also performed in this study. As shown in Figure S13, both in the normal and STF conditions, the numbers of different hemocytes and the

levels of all blood markers in the mice treated with Dox or Dox-RM-LPs were comparable to those of the control mice injected with PBS, revealing a great safety of the proposed therapeutic schedule.

Biodistribution Profile and Biosafety of RM-LPs. Additionally, we evaluated the biodistribution profile and biosafety of RM-LPs in vivo. The DiR-labeled RM-LPs were i.v. injected into mice under normal and STF conditions, followed by fluorescence detection of the main organs, including the liver, heart, lung, kidneys, spleen, and brain. As shown in Figure 7A,B and Figure S14, the RM-LPs are mainly distributed in the liver rather than the spleen, two primary organs of the reticuloendothelial system. In addition, the fluorescence intensity of main organs in STF-treated mice was slightly lower than that in the normal groups. To assess the potential adverse effects, we injected 20 mg/kg RM-LPs into the biosafety studies. Hematology and blood biochemistry assessments were performed in the mice on the seventh day of the RM-LP injection. It showed a comparable number of hemocytes, including white blood cells (WBC), RBC, and platelets (PLT), in the mice treated with either RM-LPs or PBS (Figure 7C). Meanwhile, all blood markers were in line with the mice in the PBS-treated group, suggesting excellent biosafety of RM-LPs in vivo (Figure 7D). The major organs

were also harvested for histological analysis with H&E staining. As shown in Figure 7E, the sections from key organs, including the liver, spleen, heart, lungs, and kidneys, revealed no pathological changes in RM-LP-treated groups when compared to those in the PBS group. Overall, these data demonstrated the excellent biocompatibility of RM-LPs as a drug carrier.

STUDY LIMITATIONS

Our work provides an approach to understanding the potential mechanisms of biomimetic nanovesicles synergizing with STF for the enhanced chemotherapy of malignant TNBC. Nevertheless, this study has some limitations that warrant further investigation in the STF-treated cells and animals. (1) Signaling pathways: Apart from aerobic glycolysis, the variations in intracellular signaling pathways between tumor and healthy cells upon fasting treatment present valuable opportunities for further research. It has been reported that fasting reduces various signaling cascades within healthy cells but not tumor cells, including the IGF1R-AKT-mTOR-S6K and cAMP-PKA pathways, 45,68 resulting in the differential stress resistance in tumor-bearing mice for improved chemotherapy and reduced side effects. (2) Immunomodulatory effects: The immune cells may also contribute to the enhanced chemotherapeutic efficacy in the STF-treated mice in this study. Preclinical studies confirmed that fasting treatments improve antitumor immunity by altering the immunosuppressive tumor microenvironment and influencing the functions of immune cells. For instance, fasting can decline the CD73 level in tumor cells to diminish the immunosuppressive M2-type macrophage polarization or downregulate heme oxygenase-1 production to relieve the inhibition of regulatory T cells on CD8+ cytotoxic T lymphocytes.⁷⁰ Further studies will be essential to fully understanding the synergistic mechanisms through which fasting enhances tumor therapy in vivo.

CONCLUSIONS

In summary, we demonstrated that combining biomimetic nanovesicles with STF therapy is an effective strategy for enhanced chemotherapy against TNBC. The integration of RBC membranes into liposomes makes the synthesis procedures much easier to facilitate subsequent large-scale production. Notably, the hydrophobic antitumor drugs can also be loaded in the phospholipid bilayer of nanovesicles, making them suitable for multiple chemotherapeutic drug delivery. Furthermore, we confirmed that STF can synergistically promote the uptake of drug-loaded nanovesicles by TNBC cells, thereby significantly improving the antitumor effect through multiple mechanisms and inhibiting the unwanted tumor metastasis. Since STF protects healthy cells but not tumor cells to chemotherapy, it helps prevent the potentially life-threatening side effects of chemotherapy while reducing the incidence of drug resistance. 71-73 In addition, both animal and clinical studies have demonstrated that different fasting strategies, including STF, fasting-mimicking diet, ketogenic diet, and intermittent fasting, might regulate patients' tolerance to hunger, which can serve as a safe, applicable, and low-cost adjunct strategy for cancer therapy. Overall, the synergizing of biomimetic nanovesicles with STF therapy offers substantial promise in advancing antitumor nanomedicines for enhanced chemotherapy of TNBC and other malignancies.

MATERIALS AND METHODS

RBC Membrane Derivation. The RBC membrane was prepared from whole blood according to protocols described previously with modifications.³⁴ In brief, mouse whole blood was collected via cardiac puncture using a syringe rinsed with 100 U/mL heparin solution. Following blood collection, the blood was transferred into tubes containing 10 U heparin/mL blood and mixed well by inversion. Whole blood was centrifuged at 1000×g for 10 min at 4 °C, following the removal of the serum and buffy coat layers from the RBC compartment. The isolated RBCs were further washed 2 times with cold $1 \times PBS$ (pH = 7.4) upon centrifugation at $500 \times g$ for 15 min at 4 °C. The washed RBCs were resuspended in 0.25 × PBS with a 5fold volume for hemolysis. The lysed RBC then underwent centrifugation at 12,000×g for 10 min. The supernatant was discarded, and the pellet was collected. Repeated washing was conducted with 0.25 × PBS until a pink pellet was obtained. Finally, the pellet was suspended in 0.2 mM ethylenediaminetetraacetic acid (EDTA) aqueous solution. The protein concentrations were determined using a bicinchoninic acid (BCA) protein assay kit. The RBC membrane was stored at -80 °C for further use.

Preparation and Characterization of NPs. Both LPs and RM-LPs were prepared using a thin-film hydration method.³⁵ Briefly, to prepare the LPs, distearoylphosphatidylcholine (DSPC), cholesterol, and 1,2-distearoyl-sn-glycero-3-phosphoethanolamine-N-[methoxy-(polyethylene glycol)2000] (DSPE-PEG₂₀₀₀) were dissolved in a chloroform:methanol (4:1, v/v) mixture at a molar ratio of 70:25:5 (mol %). The organic solvent was evaporated in a round-bottom flask through an RV10 rotary evaporator (IKA, Germany) under reduced pressure at 40 °C until a thin film was formed. The lipid film was then hydrated with ultrapure water (0.5 mg/mL) in a water bath at 60 °C for 5 min and sonicated for 1 min (100 mW, 42 kHz) in a bath sonicator (Scientz, China). This procedure was repeated for three cycles. For the preparation of RM-LPs or RM, 10 wt % RBC membranes were incubated with the hydrated lipid components or added in ultrapure water for 10-fold dilution, following the sonication in an ice-cold water bath for 10 min. Both LPs, RM, and RM-LPs were sequentially extruded through 200 and 100 nm polycarbonate membranes (Whatman, UK) for 10 cycles using a manual extruder (Avanti Polar Lipids, Germany). The particle size and surface zeta potential (ξ) were analyzed with dynamic light scattering (DLS, Malvern Zetasizer Nano, UK). The protein profiles of RM and RM-LPs were determined using SDS-PAGE. In summary, samples were prepared at a protein concentration of 1.3 mg/mL in an SDS loading buffer. All samples were heated to 90 °C for 5 min and then loaded onto a 10% SDS-polyacrylamide gel. Electrophoresis was carried out in the SDS running buffer and ran at 120 V for 2 h. The resulting gel was stained with Coomassie blue buffer, and the images were captured with a GL-800 white light transmissometer (Kylin-Bell, China).

Cryogenic Electron Microscopy (Cryo-EM). Carbon-coated copper grid (400 mesh, Holey) was glow-discharged in an argon and oxygen atmosphere for 10 s on the carbon side (PELCO easyGlow, Agar Scientific, USA). The RM-LPs (5 μL, 5 mg/mL in water) were carefully dropped onto the grid and blotted in a 100% humidity chamber at 20 °C for 5 s. The grid was plunge-frozen into liquid ethane and cooled by liquid nitrogen using a Vitrobot Mark IV System (EM GP2, Leica, Germany). Imaging was then recorded on a Talos F200C G2 transmission electron microscope (FEI, USA) operating at 200 kV on a CCD camera (4K × 4K, Gatan, USA).

Drug Loading and Release Studies. To prepare the Dox-loaded RM-LPs, Dox was mixed with hydrated lipid solution at different weight ratios and prepared according to the same NP formulation procedure described above. Dox-RM-LPs were washed twice to remove excess drug molecules using the Amicon Centrifugal Filter (100 kDa molecular weight cutoff, MWCO). To measure the encapsulation efficiency (calculated by dividing the weight of encapsulated drug by the input drug weight) and loading capacity (calculated by dividing the weight of encapsulated drug by the total NPs weight), the Dox concentration was determined through UV absorbance at 480 nm using a microplate reader (Tecan). Known

concentrations of Dox (0–400 μ g/mL) were used to generate a standard curve. In the drug release studies, 500 μ L of Dox-RM-LPs (0.5 mg/mL in PBS) were loaded into standard regenerated cellulose dialysis tubing with an MWCO of 3500 kDa and clipped by standard closures. The dialysis tubing was immersed into 10 mL of release medium (10 mM PBS, pH 7.4) at 37 °C with agitation at 100 rpm. To measure the sequential drug release profile, drops of hydrochloric acid (1 mM in water) were added to the release buffer at 4 and 8 h to decrease the pH values to 6.8 and 5.0, respectively. At different time points, 200 uL of the dissolution medium was withdrawn and replaced with an equal volume of the fresh medium. The cumulative drug release profile was analyzed based on the absorbance of Dox at 480 nm using a microplate reader (Tecan).

Phagocytosis Study. LPs and RM-LPs were labeled with 1,1'dioctadecyl-3,3,3',3'-tetramethylindotricarbocyanine iodide (DiR, 2 wt %, excitation/emission = 750/780 nm) for fluorescence analysis based on the hydration procedure above. CD47-blocked RM-LPs were prepared by preincubating the DiR-loaded RM-LPs (50 µg) with antimouse CD47 antibodies (20 μ g, biolegend) for 1 h and washed with 1 × PBS. To study the phagocytic capacity of macrophages, the murine macrophage, RAW264.7 cell line, was cultured in Dulbecco's Modified Eagle's Medium (DMEM) supplemented with 10% FBS, 100 mg/mL streptomycin, and 100 U/mL penicillin (all from Gibco). The cells were seeded in a 12-well plate at a density of 5×10^5 cells per well and maintained at 37 °C with 5% CO₂ in a humiditycontrolled incubator for 24 h. Different concentrations of DiR-labeled NPs $(0-200 \mu g/mL)$ were incubated with RAW264.7 cells for 4 h. After washing with 1 × PBS, the DiR-positive cells were collected and analyzed with a CytoFLEX flow cytometer (Beckman, US). The median fluorescence intensity (MFI) results were calculated using the FlowJo software.

Cellular Uptake of Dox-RM-LPs. The 4T1 murine breast cancer cell line was cultured in an RPMI 1640 medium supplemented with 10% FBS and 1% penicillin-streptomycin (37 °C, 5% CO₂). To study the cellular uptake efficiency of RM-LPs in normal and STF conditions, 4T1 cells were first seeded overnight in a 6-well plate at a density of 2×10^5 cells per well. For STF pretreatment, the cell culture medium was switched from a normal RPMI 1640 medium (2 g/L of glucose and 10% FBS) to a fasting medium (0.5 g/L of glucose and 1% of FBS) for 24 h. Afterward, different concentrations of 2 wt% DiR-labeled RM-LPs (0–400 μ g/mL) were incubated with 4T1 cells in the normal and STF medium for 4 h. The cells were then harvested using 0.25% trypsin-EDTA, washed with 1 × PBS, and analyzed with a CytoFLEX flow cytometer. To investigate the potential mechanism of RM-LPs uptake in normal and STF conditions, different endocytosis pathway inhibitors, including chlorpromazine (CPZ, 30 μ M), methyl- β -cyclodextrin (M β CD, 5 mM), and amiloride hydrochloride (AH, 50 μ M), were preincubated with 4T1 cells for 1 h, followed by the treatment of DiR-labeled RM-LPs (200 μ g/mL) for 4 h. The DiR-positive cells were then harvested and detected by a flow cytometer. Results were analyzed using the FlowJo software.

To visualize the intracellular uptake of NPs, the 4T1 cells were seeded overnight on a confocal dish (1 \times 10⁵ cells/well) prior to pretreatment with normal and the STF medium for an additional 24 h. The Dox-RM-LPs were first stained with a lysosome membranetargeting fluorogenic probe, benzoselenadiazole-modified conjugated oligoelectrolytes (COE-BSe, 2.5 μ M, 10 mM stock in DMSO) for visualization of the RM-LPs. The COE-BSe is a water-soluble dye with weak fluorescence but has strong fluorescence emission when inserted into the lipid bilayer of the RM-LPs. 75 After being washed twice with 1 × PBS, the COE-BSe-labeled Dox-RM-LPs (Dox concentration of 4 μ M) were added to the cells and incubated for 4 h. Free RM-LPs were removed by washing twice with $1 \times PBS$. The cells were then costained with lysosome tracker green (50 nM) and Hoechst 33342 (2 μ g/mL) for 30 min. The living cells were rinsed twice carefully with 1 × PBS and maintained in Hanks' Balanced Salt Solution (HBSS). The cell imaging was performed using a STELLARIS 5 confocal microscope (Leica, Germany) to visualize the nucleus by Hoechst 33342 (excitation/emission = 350 nm/460 nm), the lysosome tracker green (excitation/emission = 500 nm/520

nm), the COE-BSe-labeled RM-LPs (excitation/emission = 563 nm/674 nm), and the Dox (excitation/emission = 480/590 nm). The colocalization curves of RM-LPs and lysosome trackers were determined using the ImageJ software.

Cell Viability and Apoptosis Studies. The 4T1 tumor cells and MODE-K health cells were first seeded and incubated overnight in a 96-well plate at a density of 1×10^4 cells per well. The cells were pretreated with either normal or the STF medium for 24 h. Different concentrations of Dox or Dox-RM-LPs (0-125 µM Dox in the normal or STF medium) were then added to the cells for 24 h treatment. The cell viability was determined by using a fluorometric Resazurin Cell Viability Assay Kit following the manufacturer's instruction (Biotium, US) and quantified by measuring the relative fluorescence signal of resazurin (~44 µM) using a fluorescence microplate reader (excitation/emission = 560 nm/590 nm). Untreated cells were used as the control group with 100% viability. For the apoptosis study, 4T1 cells with or without STF pretreatment were seeded in a 6-well plate at the density of 2×10^5 cells per well. After an overnight incubation, cells were incubated with Dox-RM-LPs or free Dox (4 μ M) for 24 h. The apoptotic cells were stained with Annexin V-FITC and propidium iodide (PI) following the standard protocol of the manufacturer (Uelandy, China) and finally determined by a flow cytometer. The percentage of late apoptotic cells (Annexin V^+/PI^+) and necrotic cells (Annexin V^-/PI^+) were analyzed using the FlowJo software.

Cellular Mechanism Studies. A total of 2×10^5 4T1 cells with or without STF pretreatment were incubated with Dox-RM-LPs or free Dox (4 µM) for cellular mechanisms studies. In the cell cycle studies, drug-treated cells were harvested and fixed with 70% ice-cold ethanol for 1 h. After washing twice with 1 × PBS, the cells were incubated with 50 μ L of ribonuclease A (100 μ g/mL, Macklin) and 300 μ L of PI solution (50 μ g/mL) for 20 min at room temperature. Cells are finally detected by a flow cytometer. For the Western blotting analysis, cells in different groups were lysed in a radioimmunoprecipitation assay (RIPA) buffer (50 mM Tris-HCl, 150 mM NaCl, 1% Nonidet P 40, 0.1% SDS, 2 μM EDTA, pH 7.4) supplemented with protease inhibitors and phosphatase inhibitors (Roche). Protein concentrations were quantified using a BCA protein assay kit. Equal amounts of proteins (20 μ g) were resolved by 10% SDS-PAGE. The gel was transferred onto a nitrocellulose membrane and stained with primary antibodies (Servicebio) specific for glucose transporter 1 (GLUT1), hexokinase 2 (HK2), pyruvate kinase isozymes M2 (PKM2), and β -actin, along with horseradish peroxidase (HRP)-conjugated secondary antibodies against mouse IgG or rabbit IgG (Biolegend).

To quantify the aerobic glycolysis of 4T1 cells under normal and STF conditions, the glucose uptake activity and intracellular lactate, glucose, and ATP levels were measured based on the commercialized assay kits. In the glucose uptake study, a fluorescent glucose tracer, 2-(N-(7-Nitrobenz-2-oxa-1,3-diazol-4-yl)amino)-2-deoxyglucose (2-NBDG), was used to monitor glucose transport in cells. Upon transport via glucose transporters (GLUTs), 2-NBDG undergoes phosphorylation at the C-6 position to give 2-NBDG-6-phosphate, which is well retained within the cells, resulting in enhanced green fluorescence. Here, the uptake capacity was assessed using the 2-NBDG glucose assay kit (APExBIO, USA) according to the manufacturer's instructions. Briefly, STF-treated 4T1 cells were incubated with Dox-RM-LPs or free Dox for 24 h. The cells were then treated with 2-NBDG (100 μ M) for 30 min at 37 °C, and the intracellular fluorescence intensity was analyzed by flow cytometry. The intracellular lactate, glucose, and ATP levels were determined in the 4T1 cell lysates from different groups (mol/mg protein) by following the manufacturer's protocols. These assays were performed using a lactate assay kit (Dojindo molecular technologies, USA), a glucose assay kit with O-toluidine (Beyotime, China), and an ATP assay kit (MedchemExpress, USA), respectively. The relative concentrations of lactate, glucose, and ATP were calculated using the standard curve and normalized in reference to 4T1 cell lysate in the control group without drugs or STF treatment. Moreover, in the oxidative stress study, drug-treated cells were collected and stained

with 150 μ L of dihydroethidium (DHE, 10 μ M, Adamas) for 30 min at room temperature. For the autophagy study, drug-treated cells were stained with monodansylcadaverine (MDC, 50 mM) at 37 °C for 15 min and washed three times with 1 × PBS, following the manufacturer's protocol of the autophagy assay kit (Yuanye, China). All staining procedures were protected from light, followed by flow cytometry analysis. Results were processed using FlowJo software.

In Vivo Pharmacokinetics and Biodistribution Studies. All of the animal procedures complied with the guidelines of the Institutional Animal Care and Use Committee (IACUC) of Shanghai Jiao Tong University, China. For the blood circulation study, 100 μ L of DiR-labeled LPs or RM-LPs (20 mg/kg, n = 3) were injected through the tail vein of BALB/c mice (8-week-old, female). A drop of blood (\sim 30 μ L) was collected from each mouse via submandibular puncture with heparin-coated tubes at 0.02, 0.25, 0.5, 1, 2, 4, 8, and 24 h postinjection. The collected blood (20 μ L) was then diluted with 1 \times PBS (180 μ L) under sonication. The fluorescence intensity of DiRlabeled NPs in the blood was measured by using a microplate reader. For the pharmacokinetics analysis, 200 μ L of free Dox or Dox-RM-LPs (20 mg Dox/kg, n = 3) were intravenously injected into the mice. The blood was collected from submandibular location (30 μ L) at the indicated time points, clotted at room temperature for 30 min, and centrifuged at 2000×g for 15 min to collect the serum. Then, 10 μ L of serum was added into 990 μ L of extraction buffer (0.075 M HCl, 90% isopropanol) for protein precipitation. The samples were stored at -20 °C for 20 min and warmed to room temperature, followed by centrifugation at 10,000×g for 15 min. The supernatants were collected for fluorescence analysis using a fluorescence microplate reader (excitation/emission = 480 nm/590 nm). The Dox concentrations were calculated from the standard curve. For the biodistribution study, fasted mice were intravenously administered with DiR-labeled RM-LPs (100 μ L, 20 mg/kg). At 24, 48, 72, and 96 h postinjection, the mice were imaged based on the In Vivo Imaging System (IVIS, PerkinElmer, US).

In Vivo Tumor Treatment Efficacy and Biosafety Studies. To develop a murine breast tumor model, 5×10^5 4T1 cells were implanted subcutaneously into the right flank of BALB/c mice (8week-old, female). Tumor volumes were measured by a caliper and calculated using the equation: volume = $(length \times width^2) / 2$. When the average tumor size reached 100 mm³, mice were fasted for 48 h with a continuous water supply only, followed by sufficient food supply for another 48 h. During the two cycles of STF and feeding treatment, the body weight and blood glucose of mice were recorded daily. To investigate the therapeutic efficacy, tumor-bearing normal mice were i.v. injected twice (day 2 and day 6) with either PBS, Dox, or Dox-RM-LPs at same drug dosage (5 mg/kg, n = 5). Fasted mice were administered with Dox-RM-LP treatment (5 mg/kg, n = 5) on the same therapeutic schedule. All mice were euthanized on day 12. Whole blood (500 μ L) was collected through cardiac puncture and allowed to coagulate in an Eppendorf tube. After centrifugation at 2000×g for 15 min, the serum was harvested for comprehensive hematology analysis. Furthermore, 300 μ L of whole blood was placed into an EDTA-coated anticoagulant tube for the complete blood count. Major organs, such as the heart, liver, spleen, lung, and kidneys, as well as tumors were collected, weighted, and fixed in 4% paraformaldehyde overnight for hematoxylin and eosin (H&E) staining. To evaluate the biosafety of the nanocarrier, BALB/c mice (8-week-old, female) were i.v. injected with PBS or RM-LPs (20 mg/ kg, n = 3). On day 7 postinjection, hematology and blood biochemistry assessments were performed in the mice following the procedures above. For histopathological examination, mice were sacrificed and their major organs, such as the heart, liver, spleen, lung, and kidney, were resected, fixed in 4% paraformaldehyde for 24 h, and sectioned for H&E staining.

Statistical Analysis. All data were presented as mean \pm standard deviations (s.d.) from at least three independent experiments. GraphPad Prism 8.0 software was applied for all graph generation and statistical analysis. Significant differences were determined using the student's two-tailed *t*-test (*p*-value: *p < 0.05, **p < 0.01, and ***p < 0.001).

ASSOCIATED CONTENT

Supporting Information

The Supporting Information is available free of charge at https://pubs.acs.org/doi/10.1021/acsnano.4c07074.

Long-term stability of RM-LPs, immune-evasive property of CD47 on RM-LPs, blood circulation profiles of RM-LPs, size and encapsulation capacity of Dox-loaded RM-LPs, drug release kinetics, quantitative analysis of cellular uptake, cytotoxicity of RM-LPs in tumor and healthy cells, intracellular glucose and ATP levels, time-dependent tumor images, pharmacokinetic study of free Dox and Dox-loaded RM-LPs, body weights of mice during treatment, H&E histological staining of main organs, blood cell amounts and blood chemistry analysis, and biodistribution of RM-LPs in vivo (PDF)

AUTHOR INFORMATION

Corresponding Authors

Haijiao Lu — Department of Respiratory and Critical Care Medicine, Shanghai Chest Hospital, School of Medicine, Shanghai Jiao Tong University, Shanghai 200030, China; Email: luhaijiao@shsmu.edu.cn

Rongxiu Li — School of Life Sciences and Biotechnology, Shanghai Jiao Tong University, Shanghai 200240, China; Email: rxli@sjtu.edu.cn

Xiangzhao Ai — School of Life Sciences and Biotechnology and Sheng Yushou Center of Cell Biology and Immunology, School of Life Sciences and Biotechnology, Shanghai Jiao Tong University, Shanghai 200240, China; orcid.org/0000-0002-7205-3748; Email: xzai@sjtu.edu.cn

Authors

Seok Theng Chiang – School of Life Sciences and Biotechnology, Shanghai Jiao Tong University, Shanghai 200240, China

Qi Chen – School of Life Sciences and Biotechnology, Shanghai Jiao Tong University, Shanghai 200240, China

Tianzhen Han – School of Life Sciences and Biotechnology, Shanghai Jiao Tong University, Shanghai 200240, China Chunxi Qian – School of Life Sciences and Biotechnology,

Shanghai Jiao Tong University, Shanghai 200240, China Xiaoshuai Shen – School of Life Sciences and Biotechnology, Shanghai Jiao Tong University, Shanghai 200240, China

Yijing Lin – Department of Obstetrics and Gynecology, Ruijin Hospital, Shanghai Jiao Tong University School of Medicine, Shanghai 200025, China

Rong Xu – School of Life Sciences and Biotechnology, Shanghai Jiao Tong University, Shanghai 200240, China

Zhongyu Cao – School of Life Sciences and Biotechnology, Shanghai Jiao Tong University, Shanghai 200240, China

Cheng Zhou — Institute of Polymer Optoelectronic Materials and Devices, State Key Laboratory of Luminescent Materials and Devices, South China University of Technology, Guangzhou 510640, China; orcid.org/0000-0003-0770-2649

Complete contact information is available at: https://pubs.acs.org/10.1021/acsnano.4c07074

Author Contributions

*S.T.C. and Q.C. contributed equally to this work. S.T.C., Q.C., H.L., R.L., and X.A. conceived and designed the experiments. S.T.C., Q.C., and X.A. performed the experiments

and analyzed the data. S.T.C., Q.C., T.H., C.Q., X.S., Y.L., R.X., Z.C., C.Z., H.L., R.L., and X.A. wrote and revised the manuscript. All authors have approved the final version of the manuscript.

Notes

The authors declare no competing financial interest.

ACKNOWLEDGMENTS

The authors gratefully thank Dr. Zhenfeng Zhang for the western blot tests and analysis. We also thank the funding support from the National Natural Science Foundation of China (grant nos. 52202180, 32271437, and 82303030), the Youth Foundation of Shanghai Municipal Health Commission (20224Y0016), and the Yangfan Program of Shanghai Municipal Science and Technology Committee (23YF1441100). The TOC and Figures ¹, ³E, ⁵H, and ⁶A in this article were created with www.BioRender.com.

REFERENCES

- (1) Bray, F.; Laversanne, M.; Sung, H.; Ferlay, J.; Siegel, R. L.; Soerjomataram, I.; Jemal, A. Global Cancer Statistics 2022: GLOBOCAN Estimates of Incidence and Mortality Worldwide for 36 Cancers in 185 Countries. *CA Cancer J. Clin.* 2024, 74 (3), 229–263.
- (2) Bianchini, G.; De Angelis, C.; Licata, L.; Gianni, L. Treatment Landscape of Triple-Negative Breast Cancer Expanded Options. *Evolving Needs. Nat. Rev. Clin. Oncol.* **2022**, 19 (2), 91–113.
- (3) Marra, A.; Trapani, D.; Viale, G.; Criscitiello, C.; Curigliano, G. Practical Classification of Triple-Negative Breast Cancer: Intratumoral Heterogeneity, Mechanisms of Drug Resistance, and Novel Therapies. *npj Breast Cancer* **2020**, *6*, 54.
- (4) Yin, Y.; Yan, Y.; Fan, B.; Huang, W.; Zhang, J.; Hu, H. Y.; Li, X.; Xiong, D.; Chou, S. L.; Xiao, Y.; et al. Novel Combination Therapy for Triple-Negative Breast Cancer based on an Intelligent Hollow Carbon Sphere. *Research* 2023, 6, No. 0098.
- (5) Guo, J.; Hu, J.; Zheng, Y.; Zhao, S.; Ma, J. Artificial Intelligence: Opportunities and Challenges in the Clinical Applications of Triple-Negative Breast Cancer. *Br. J. Cancer* **2023**, *128* (12), 2141–2149.
- (6) Bianchini, G.; Balko, J. M.; Mayer, I. A.; Sanders, M. E.; Gianni, L. Triple-Negative Breast Cancer: Challenges and Opportunities of a Heterogeneous Disease. *Nat. Rev. Clin. Oncol.* **2016**, *13* (11), 674–690.
- (7) Amir, E.; Ocana, A.; Freedman, O.; Clemons, M.; Seruga, B. Chemotherapy: Dose-Dense Treatment for Triple-Negative Breast Cancer. *Nat. Rev. Clin. Oncol.* **2010**, *7* (2), 79–80.
- (8) Rodenhuis, S.; Bontenbal, M.; van Hoesel, Q. G.; Smit, W. M.; Nooij, M. A.; Voest, E. E.; van der Wall, E.; Hupperets, P.; van Tinteren, H.; Peterse, J. L.; et al. Efficacy of High-Dose Alkylating Chemotherapy in HER2/Neu-Negative Breast Cancer. *Ann. Oncol.* **2006**, *17* (4), 588–596.
- (9) Lin, A.; Giuliano, C. J.; Palladino, A.; John, K. M.; Abramowicz, C.; Yuan, M. L.; Sausville, E. L.; Lukow, D. A.; Liu, L.; Chait, A. R.; et al. Off-Target Toxicity is a Common Mechanism of Action of Cancer Drugs Undergoing Clinical Trials. *Sci. Transl. Med.* **2019**, *11* (509), No. eaaw8412.
- (10) Abumanhal-Masarweh, H.; da Silva, D.; Poley, M.; Zinger, A.; Goldman, E.; Krinsky, N.; Kleiner, R.; Shenbach, G.; Schroeder, J. E.; Shklover, J.; et al. Tailoring the Lipid Composition of Nanoparticles Modulates Their Cellular Uptake and Affects the Viability of Triple Negative Breast Cancer Cells. *J. Controlled Release* **2019**, 307, 331–341.
- (11) Pateras, I. S.; Williams, C.; Gianniou, D. D.; Margetis, A. T.; Avgeris, M.; Rousakis, P.; Legaki, A.-I.; Mirtschink, P.; Zhang, W.; Panoutsopoulou, K.; et al. Short Term Starvation Potentiates the Efficacy of Chemotherapy in Triple Negative Breast Cancer *via* Metabolic Reprogramming. *J. Transl. Med.* 2023, 21 (1), 169.

- (12) Krishnan, N.; Jiang, Y.; Zhou, J.; Mohapatra, A.; Peng, F.-X.; Duan, Y.; Holay, M.; Chekuri, S.; Guo, Z.; Gao, W.; et al. A Modular Approach to Enhancing Cell Membrane-Coated Nanoparticle Functionality Using Genetic Engineering. *Nat. Nanotechnol.* **2024**, 19 (3), 345–353.
- (13) Liu, C.; Liu, X.; Xiang, X.; Pang, X.; Chen, S.; Zhang, Y.; Ren, E.; Zhang, L.; Liu, X.; Lv, P.; et al. A Nanovaccine for Antigen Self-Presentation and Immunosuppression Reversal as a Personalized Cancer Immunotherapy Strategy. *Nat. Nanotechnol.* **2022**, *17* (5), 531–540.
- (14) Wei, X.; Wang, Y.; Liu, Y.; Ji, K.; Li, K.; Wang, J.; Gu, Z. Biomimetic Design Strategies for Biomedical Applications. *Matter* **2024**, 7 (3), 826–854.
- (15) Liu, W. L.; Zou, M. Z.; Liu, T.; Zeng, J. Y.; Li, X.; Yu, W. Y.; Li, C. X.; Ye, J. J.; Song, W.; Feng, J.; et al. Cytomembrane Nanovaccines Show Therapeutic Effects by Mimicking Tumor Cells and Antigen Presenting Cells. *Nat. Commun.* **2019**, *10* (1), 3199.
- (16) Li, Z.; Wang, Z.; Dinh, P.-U. C.; Zhu, D.; Popowski, K. D.; Lutz, H.; Hu, S.; Lewis, M. G.; Cook, A.; Andersen, H.; et al. Cellmimicking Nanodecoys Neutralize SARS-CoV-2 and Mitigate Lung Injury in a Non-Human Primate Model of COVID-19. *Nat. Nanotechnol.* **2021**, *16* (8), 942–951.
- (17) Ai, X.; Wang, D.; Honko, A.; Duan, Y.; Gavrish, I.; Fang, R. H.; Griffiths, A.; Gao, W.; Zhang, L. Surface Glycan Modification of Cellular Nanosponges to Promote SARS-CoV-2 Inhibition. *J. Am. Chem. Soc.* **2021**, 143 (42), 17615–17621.
- (18) Xu, J.; Ma, Q.; Zhang, Y.; Fei, Z.; Sun, Y.; Fan, Q.; Liu, B.; Bai, J.; Yu, Y.; Chu, J.; et al. Yeast-Derived Nanoparticles Remodel the Immunosuppressive Microenvironment in Tumor and Tumor-Draining Lymph Nodes to Suppress Tumor Growth. *Nat. Commun.* 2022, 13 (1), 110.
- (19) Chen, L.; Zhao, R.; Shen, J.; Liu, N.; Zheng, Z.; Miao, Y.; Zhu, J.; Zhang, L.; Wang, Y.; Fang, H.; et al. Antibacterial Fusobacterium Nucleatum-Mimicking Nanomedicine to Selectively Eliminate Tumor-Colonized Bacteria and Enhance Immunotherapy Against Colorectal Cancer. *Adv. Mater.* **2023**, *35* (45), No. 2306281.
- (20) Ai, X.; Wang, D.; Noh, I.; Duan, Y.; Zhou, Z.; Mukundan, N.; Fang, R. H.; Gao, W.; Zhang, L. Glycan-Modified Cellular Nanosponges for Enhanced Neutralization Of Botulinum Toxin. *Biomaterials* **2023**, *302*, No. 122330.
- (21) Han, Y.; Pan, H.; Li, W.; Chen, Z.; Ma, A.; Yin, T.; Liang, R.; Chen, F.; Ma, Y.; Jin, Y.; et al. T Cell Membrane Mimicking Nanoparticles with Bioorthogonal Targeting and Immune Recognition for Enhanced Photothermal Therapy. *Adv. Sci.* **2019**, *6* (15), No. 1900251.
- (22) Zhai, Y.; Wang, J.; Lang, T.; Kong, Y.; Rong, R.; Cai, Y.; Ran, W.; Xiong, F.; Zheng, C.; Wang, Y.; et al. T Lymphocyte Membrane-Decorated Epigenetic Nanoinducer of Interferons for Cancer Immunotherapy. *Nat. Nanotechnol.* **2021**, *16* (11), 1271–1280.
- (23) Li, J.; Zhen, X.; Lyu, Y.; Jiang, Y.; Huang, J.; Pu, K. Cell Membrane Coated Semiconducting Polymer Nanoparticles for Enhanced Multimodal Cancer Phototheranostics. *ACS Nano* **2018**, 12 (8), 8520–8530.
- (24) Zhou, Q.; Shao, S.; Wang, J.; Xu, C.; Xiang, J.; Piao, Y.; Zhou, Z.; Yu, Q.; Tang, J.; Liu, X.; et al. Enzyme-Activatable Polymer-Drug Conjugate Augments Tumour Penetration and Treatment Efficacy. *Nat. Nanotechnol.* **2019**, *14* (8), 799–809.
- (25) Nichols, J. W.; Bae, Y. H. Odyssey of a Cancer Nanoparticle: From Injection Site to Site of Action. *Nano Today* **2012**, *7* (6), 606–618.
- (26) Li, J.; Wu, Y.; Wang, J.; Xu, X.; Zhang, A.; Li, Y.; Zhang, Z. Macrophage Membrane-Coated Nano-Gemcitabine Promotes Lymphocyte Infiltration and Synergizes AntiPD-L1 to Restore the Tumoricidal Function. ACS Nano 2023, 17 (1), 322–336.
- (27) Fang, R. H.; Gao, W.; Zhang, L. Targeting Drugs to Tumours Using Cell Membrane-Coated Nanoparticles. *Nat. Rev. Clin. Oncol.* **2023**, 20 (1), 33–48.

- (28) Zhang, J.; Pan, Y.; Liu, L.; Xu, Y.; Zhao, C.; Liu, W.; Rao, L. Genetically Edited Cascade Nanozymes for Cancer Immunotherapy. ACS Nano 2024, 18 (19), 12295–12310.
- (29) Yoo, J. W.; Irvine, D. J.; Discher, D. E.; Mitragotri, S. Bio-Inspired, Bioengineered and Biomimetic Drug Delivery Carriers. *Nat. Rev. Drug Discovery* **2011**, *10* (7), 521–535.
- (30) Oldenborg, P. A.; Zheleznyak, A.; Fang, Y. F.; Lagenaur, C. F.; Gresham, H. D.; Lindberg, F. P. Role of CD47 as a Marker of Self on Red Blood Cells. *Science* **2000**, 288 (5473), 2051–2054.
- (31) Chen, Q.; Wang, C.; Zhang, X.; Chen, G.; Hu, Q.; Li, H.; Wang, J.; Wen, D.; Zhang, Y.; Lu, Y.; et al. In Situ Sprayed Bioresponsive Immunotherapeutic Gel for Post-Surgical Cancer Treatment. *Nat. Nanotechnol.* **2019**, *14* (1), 89–97.
- (32) Hu, C. M.; Fang, R. H.; Copp, J.; Luk, B. T.; Zhang, L. A Biomimetic Nanosponge that Absorbs Pore-Forming Toxins. *Nat. Nanotechnol.* **2013**, *8* (5), 336–340.
- (33) Zhang, Y.; Liao, Y.; Tang, Q.; Lin, J.; Huang, P. Biomimetic Nanoemulsion for Synergistic Photodynamic-Immunotherapy Against Hypoxic Breast Tumor. *Angew. Chem., Int. Ed.* **2021**, *60* (19), 10647–10653.
- (34) Hu, C. M.; Zhang, L.; Aryal, S.; Cheung, C.; Fang, R. H.; Zhang, L. Erythrocyte Membrane-Camouflaged Polymeric Nanoparticles as a Biomimetic Delivery Platform. *Proc. Natl. Acad. Sci. U.S.A.* **2011**, *108* (27), 10980–10985.
- (35) He, Y.; Li, R.; Li, H.; Zhang, S.; Dai, W.; Wu, Q.; Jiang, L.; Zheng, Z.; Shen, S.; Chen, X.; et al. Erythroliposomes: Integrated Hybrid Nanovesicles Composed of Erythrocyte Membranes and Artificial Lipid Membranes for Pore-Forming Toxin Clearance. *ACS Nano* 2019, 13 (4), 4148–4159.
- (36) Chen, S.; Fan, J.; Xiao, F.; Qin, Y.; Long, Y.; Yuan, L.; Liu, B. Erythrocyte Membrane-Camouflaged Prussian Blue Nanocomplexes for Combinational Therapy of Triple-Negative Breast Cancer. *J. Mater. Chem. B* **2023**, *11* (10), 2219–2233.
- (37) Ai, X.; Wang, S.; Duan, Y.; Zhang, Q.; Chen, M. S.; Gao, W.; Zhang, L. Emerging Approaches to Functionalizing Cell Membrane-Coated Nanoparticles. *Biochemistry* **2021**, *60* (13), 941–955.
- (38) Mindikoglu, A. L.; Abdulsada, M. M.; Jain, A.; Jalal, P. K.; Devaraj, S.; Wilhelm, Z. R.; Opekun, A. R.; Jung, S. Y. Intermittent Fasting from Dawn to Sunset for Four Consecutive Weeks Induces Anticancer Serum Proteome Response and Improves Metabolic Syndrome. Sci. Rep. 2020, 10 (1), 18341.
- (39) Wei, S.; Han, R.; Zhao, J.; Wang, S.; Huang, M.; Wang, Y.; Chen, Y. Intermittent Administration of a Fasting-Mimicking Diet Intervenes in Diabetes Progression, Restores B Cells and Reconstructs Gut Microbiota in Mice. *Nutr. Metab.* **2018**, *15*, 80.
- (40) Vernieri, C.; Ligorio, F.; Zattarin, E.; Rivoltini, L.; De Braud, F. Fasting-Mimicking Diet Plus Chemotherapy in Breast Cancer Treatment. *Nat. Commun.* **2020**, *11* (1), 4274.
- (41) Kanarek, N.; Petrova, B.; Sabatini, D. M. Dietary Modifications for Enhanced Cancer Therapy. *Nature* **2020**, *579* (7800), 507–517.
- (42) Caffa, I.; Spagnolo, V.; Vernieri, C.; Valdemarin, F.; Becherini, P.; Wei, M.; Brandhorst, S.; Zucal, C.; Driehuis, E.; Ferrando, L.; et al. Fasting-Mimicking Diet and Hormone Therapy Induce Breast Cancer Regression. *Nature* **2020**, *583* (7817), 620–624.
- (43) de Gruil, N.; Pijl, H.; van der Burg, S. H.; Kroep, J. R. Short-Term Fasting Synergizes with Solid Cancer Therapy by Boosting Antitumor Immunity. *Cancers* **2022**, *14* (6), 1390.
- (44) Raffaghello, L.; Lee, C.; Safdie, F. M.; Wei, M.; Madia, F.; Bianchi, G.; Longo, V. D. Starvation-Dependent Differential Stress Resistance Protects Normal but not Cancer Cells Against High-Dose Chemotherapy. *Proc. Natl. Acad. Sci. U.S.A.* **2008**, *105* (24), 8215–8220
- (45) Lee, C.; Safdie, F. M.; Raffaghello, L.; Wei, M.; Madia, F.; Parrella, E.; Hwang, D.; Cohen, P.; Bianchi, G.; Longo, V. D. Reduced Levels of IGF-I Mediate Differential Protection of Normal and Cancer Cells in Response to Fasting and Improve Chemotherapeutic Index. *Cancer Res.* **2010**, *70* (4), 1564–1572.
- (46) Salvadori, G.; Zanardi, F.; Iannelli, F.; Lobefaro, R.; Vernieri, C.; Longo, V. D. Fasting-Mimicking Diet Blocks Triple-Negative

- Breast Cancer and Cancer Stem Cell Escape. Cell Metab. 2021, 33 (11), 2247–2259.
- (47) Cortellino, S.; Quagliariello, V.; Delfanti, G.; Blaževitš, O.; Chiodoni, C.; Maurea, N.; Di Mauro, A.; Tatangelo, F.; Pisati, F.; Shmahala, A.; et al. Fasting Mimicking Diet in Mice Delays Cancer Growth and Reduces Immunotherapy-Associated Cardiovascular and Systemic Side Effects. *Nat. Commun.* 2023, 14 (1), 5529.
- (48) Cheng, H.; Jiang, X. Y.; Zheng, R. R.; Zuo, S. J.; Zhao, L. P.; Fan, G. L.; Xie, B. R.; Yu, X. Y.; Li, S. Y.; Zhang, X. Z. A Biomimetic Cascade Nanoreactor for Tumor Targeted Starvation Therapy-Amplified Chemotherapy. *Biomaterials* **2019**, 195, 75–85.
- (49) Su, W.; Tan, M.; Wang, Z.; Zhang, J.; Huang, W.; Song, H.; Wang, X.; Ran, H.; Gao, Y.; Nie, G.; et al. Targeted Degradation of PD-L1 and Activation of the STING Pathway by Carbon-Dot-Based PROTACs for Cancer Immunotherapy. *Angew. Chem., Int. Ed.* **2023**, 62 (11), No. e202218128.
- (50) Lee, C.; Raffaghello, L.; Brandhorst, S.; Safdie, F. M.; Bianchi, G.; Martin-Montalvo, A.; Pistoia, V.; Wei, M.; Hwang, S.; Merlino, A.; et al. Fasting Cycles Retard Growth of Tumors and Sensitize a Range of Cancer Cell Types to Chemotherapy. *Sci. Transl. Med.* **2012**, *4* (124), 124ra27.
- (51) Nencioni, A.; Caffa, I.; Cortellino, S.; Longo, V. D. Fasting and Cancer: Molecular Mechanisms and Clinical Application. *Nat. Rev. Cancer* **2018**, *18* (11), 707–719.
- (52) Tang, X.; Li, G.; Shi, L.; Su, F.; Qian, M.; Liu, Z.; Meng, Y.; Sun, S.; Li, J.; Liu, B. Combined Intermittent Fasting and ERK Inhibition Enhance the Anti-Tumor Effects of Chemotherapy via the GSK3 β -SIRT7 Axis. *Nat. Commun.* **2021**, 12 (1), 5058.
- (53) Hay, N. Reprogramming Glucose Metabolism in Cancer: Can it be Exploited for Cancer Therapy? *Nat. Rev. Cancer* **2016**, *16* (10), 635–649.
- (54) Martínez-Reyes, I.; Chandel, N. S. Cancer Metabolism: Looking Forward. *Nat. Rev. Cancer* **2021**, 21 (10), 669–680.
- (55) Bianchi, G.; Martella, R.; Ravera, S.; Marini, C.; Capitanio, S.; Orengo, A.; Emionite, L.; Lavarello, C.; Amaro, A.; Petretto, A.; et al. Fasting Induces Anti-Warburg Effect that Increases Respiration but Reduces ATP-Synthesis to Promote Apoptosis in Colon Cancer Models. *Oncotarget* **2015**, *6* (14), 11806–11819.
- (56) Weng, M. L.; Chen, W. K.; Chen, X. Y.; Lu, H.; Sun, Z. R.; Yu, Q.; Sun, P. F.; Xu, Y. J.; Zhu, M. M.; Jiang, N.; et al. Fasting Inhibits Aerobic Glycolysis and Proliferation in Colorectal Cancer *via* the Fdft1-mediated AKT/mTOR/HIF1 α Pathway Suppression. *Nat. Commun.* **2020**, *11* (1), 1869.
- (57) De Groot, S.; Pijl, H.; Van der Hoeven, J. J. M.; Kroep, J. R. Effects of Short-Term Fasting on Cancer Treatment. *J. Exp. Clin. Cancer Res.* **2019**, 38 (1), 209.
- (58) Xia, Q.; Zhang, Y.; Li, Z.; Hou, X.; Feng, N. Red blood cell Membrane-Camouflaged Nanoparticles: a Novel Drug Delivery System for Antitumor Application. *Acta Pharm. Sin. B* **2019**, 9 (4), 675–689.
- (59) Lee, R. J.; Wang, S.; Turk, M. J.; Low, P. S. The Effects of pH and Intraliposomal Buffer Strength on the Rate of Liposome Content Release and Intracellular Drug Delivery. *Biosci. Rep.* **1998**, *18* (2), 69–78.
- (60) Siepmann, J.; Peppas, N. A. Higuchi Equation: Derivation, Applications, Use and Misuse. *Int. J. Pharm.* **2011**, 418 (1), 6–12.
- (61) Sousa de Almeida, M.; Susnik, E.; Drasler, B.; Taladriz-Blanco, P.; Petri-Fink, A.; Rothen-Rutishauser, B. Understanding Nanoparticle Endocytosis to Improve Targeting Strategies in Nanomedicine. *Chem. Soc. Rev.* **2021**, *50* (9), 5397–5434.
- (62) Liu, L.; Brown, D.; McKee, M.; LeBrasseur, N. K.; Yang, D.; Albrecht, K. H.; Ravid, K.; Pilch, P. F. Deletion of Cavin/PTRF Causes Global Loss of Caveolae, Dyslipidemia, and Glucose Intolerance. *Cell Metab.* **2008**, 8 (4), 310–317.
- (63) Becker, S.; Momoh, J.; Biancacci, I.; Möckel, D.; Wang, Q.; May, J. N.; Su, H.; Candels, L. S.; Berres, M. L.; Kiessling, F.; et al. Intermittent Fasting Primes the Tumor Microenvironment and Improves Nanomedicine Delivery in Hepatocellular Carcinoma. *Small* 2023, 19 (4), No. 2208042.

- (64) Matthews, H. K.; Bertoli, C.; de Bruin, R. A. M. Cell Cycle Control in Cancer. *Nat. Rev. Mol. Cell Biol.* 2022, 23 (1), 74–88.
- (65) Qian, R.; Cao, G.; Su, W.; Zhang, J.; Jiang, Y.; Song, H.; Jia, F.; Wang, H. Enhanced Sensitivity of Tumor Cells to Autophagy Inhibitors Using Fasting-Mimicking Diet and Targeted Lysosomal Delivery Nanoplatform. *Nano Lett.* **2022**, 22 (22), 9154–9162.
- (66) Song, H.; Huang, W.; Jia, F.; Wang, Z.; Zhang, J.; Qian, R.; Nie, G.; Wang, H. Targeted Degradation of Signal Transduction and Activator of Transcription 3 by Chaperone-Mediated Autophagy Targeting Chimeric Nanoplatform. ACS Nano 2024, 18 (2), 1599–1610.
- (67) Dawidczyk, C. M.; Russell, L. M.; Hultz, M.; Searson, P. C. Tumor Accumulation of Liposomal Doxorubicin in Three Murine Models: Optimizing Delivery Efficiency. *Nanomed. Nanotechnol. Biol. Med.* **2017**, *13* (5), 1637–1644.
- (68) Cheng, C.-W.; Adams, G. B.; Perin, L.; Wei, M.; Zhou, X.; Lam, B. S.; Da Sacco, S.; Mirisola, M.; Quinn, D. I.; Dorff, T. B.; et al. Prolonged Fasting Reduces IGF-1/PKA to Promote Hematopoietic-Stem-Cell-Based Regeneration and Reverse Immunosuppression. *Cell Stem Cell* **2014**, *14* (6), 810–823.
- (69) Sun, P.; Wang, H.; He, Z.; Chen, X.; Wu, Q.; Chen, W.; Sun, Z.; Weng, M.; Zhu, M.; Ma, D.; et al. Fasting Inhibits Colorectal Cancer Growth by Reducing M2 Polarization of Tumor-Associated Macrophages. *Oncotarget* 2017, 8 (43), 74649–74660.
- (70) Di Biase, S.; Lee, C.; Brandhorst, S.; Manes, B.; Buono, R.; Cheng, C.-W.; Cacciottolo, M.; Martin-Montalvo, A.; de Cabo, R.; Wei, M.; et al. Fasting-Mimicking Diet Reduces HO-1 to Promote T Cell-Mediated Tumor Cytotoxicity. *Cancer Cell* **2016**, *30* (1), 136–146.
- (71) Zhang, J.; Yin, Y.; Zhang, J.; Zhang, J.; Su, W.; Ma, H.; Jia, F.; Zhao, G.; Wang, H. Suppression of Energy Metabolism in Cancer Cells with Nutrient-Sensing Nanodrugs. *Nano Lett.* **2022**, 22 (6), 2514–2520.
- (72) Zhang, J.; Li, X.; Yin, Y.; Cao, G.; Wang, H. A Biodegradable Nucleotide Coordination Polymer for Enhanced NSCLC Therapy in Combination with Metabolic Modulation. *Adv. Healthcare Mater.* **2023**, *12* (29), No. 2302187.
- (73) Cao, G.; Tan, M.; Huang, W.; Zhang, J.; Yin, Y.; Li, X.; Ma, H.; Su, W.; Li, S.; Ran, H.; et al. Nutrient-Sensing Nanoprotoplast Augments Tumor Accumulation and Immune Response with Short-Term Starvation. *Nano Today* **2023**, *49*, No. 101762.
- (74) Zhong, Z.; Zhang, H.; Nan, K.; Zhong, J.; Wu, Q.; Lu, L.; Yue, Y.; Zhang, Z.; Guo, M.; Wang, Z.; et al. Fasting-Mimicking Diet Drives Antitumor Immunity against Colorectal Cancer by Reducing IgA-Producing Cells. *Cancer Res.* **2023**, *83* (21), 3529–3543.
- (75) Zhou, C.; Cox-Vázquez, S. J.; Chia, G. W. N.; Vázquez, R. J.; Lai, H. Y.; Chan, S. J. W.; Limwongyut, J.; Bazan, G. C. Water-Soluble Extracellular Vesicle Probes based on Conjugated Oligoelectrolytes. *Sci. Adv.* 2023, 9 (2), No. eade2996.